CHAPTER 2

ADVANCED PULSE EPR METHODS FOR THE CHARACTERIZATION OF METALLOPROTEINS

Jeffrey Harmer, George Mitrikas, and Arthur Schweiger
Laboratory of Physical Chemistry, Department of Chemistry and Applied Biosciences, ETH-Zürich, Switzerland

Electron Spin Echo Envelope Modulation (ESEEM) and pulse Electron Nuclear Double Resonance (ENDOR) experiments are considered to be two cornerstones of pulse EPR spectroscopy. These techniques are typically used to obtain the static spin Hamiltonian parameters of powders, frozen solutions, and single crystals. The development of new methods based on these two effects is mainly driven by the need for higher resolution, and therefore, a more accurate estimation of the magnetic parameters. In this chapter, we describe the inner workings of ESEEM and pulse ENDOR experiments as well as the latest developments aimed at resolution and sensitivity enhancement. The advantages and limitations of these techniques are demonstrated through examples found in the literature, with an emphasis on systems of biological relevance.

1. INTRODUCTION

During the last decades, electron paramagnetic resonance (EPR) has become a powerful spectroscopic method for studying compounds containing paramagnetic species. Applications abound in the study of transition metal complexes, organic and inorganic radicals, and paramagnetic metalloproteins. In biological systems containing one or more unpaired electrons, EPR spectroscopy can provide unique information on the electronic and geometric structure since magnetic data such as *g*-values, hyperfine couplings, and nuclear quadrupole parameters are directly related to the electronic wavefunction and the local environment of the paramagnetic center. The *g*-values and, for species with several unpaired electrons ($S > ½$), the zero-field splitting often provide fingerprint information on the type of paramagnetic species. The hyperfine couplings characterize the spin density distribution in detail and can give access to distances between the nuclei and the unpaired electron up to approximately 1 nm. The nuclear quadrupole interactions provide information on the bonding of nuclei and can also be utilized to determine bond angles. For

G. Hanson, L. Berliner (eds.), *High Resolution EPR*, Biological Magnetic Resonance 28,
DOI 10.1007/978-0-387-84856-3_2,

these reasons, EPR spectroscopy is well suited for structural studies in systems lacking long-range order on length scales that are not easily accessible by other techniques.

In powders, frozen solutions and even single crystals, many of the hyperfine and nuclear quadrupole splittings are typically not resolved in the field-swept EPR spectrum due to inhomogeneous broadening effects. In transition metal complexes, for example, often only the largest hyperfine coupling from the metal ion is observed. This lack of resolution is mainly due to the transition selection rules, which show that the number of EPR lines increases multiplicatively, $N_{\mathrm{EPR}} = \prod_k (2I_k + 1)$, where the product is over the total number of nuclei (k) with spin quantum numbers $I_k > 0$. The resolution limitation in field-swept EPR methods can be overcome by measuring nuclear frequency spectra directly with pulse techniques. In this case the number of lines increases in an additive way, $N_{\mathrm{NF}} = \sum_k I_k$. By directly measuring nuclear frequency spectra, EPR spectroscopy can access both strong and very weak interactions and, consequently, characterize the system under study in more detail.

The pulse EPR methods discussed here for measuring nuclear transition frequencies can be classified into two categories. The first involves using electron nuclear double resonance (ENDOR) techniques where the signal arises from the excitation of EPR and NMR transitions by microwave (m.w.) and radiofrequency (r.f.) irradiation, respectively. In the second class of experiments, based on the electron spin echo envelope modulation (ESEEM) effect, the nuclear transition frequencies are indirectly measured by the creation and detection of electron or nuclear coherences using only m.w. pulses. No r.f. irradiation is required. ENDOR and ESEEM spectra often give complementary information. ENDOR experiments are especially suited for measuring nuclear frequencies above approximately 5 MHz, and are often most sensitive when the hyperfine interaction in not very anisotropic. Conversely, anisotropic interactions are required for an ESEEM effect, and the technique can easily measure low nuclear frequencies.

Following the rapid development of pulse EPR spectroscopy during the last few decades, pulse EPR methods based on ENDOR and ESEEM effects have been successfully applied to characterize paramagnetic systems containing transition metal ions [1–6]. Together with this ever-increasing number of applications, there is an ongoing effort to develop new methods aimed at resolution and/or sensitivity enhancement [7]. Nowadays, there is a large variety of pulse EPR experiments that can specifically address a given problem and provide optimum resolution. Furthermore, results from such advanced experiments are often more easily interpreted because fewer assumptions are required. The aim of this contribution is to give an up-to-date overview of the existing pulse EPR experiments based on ENDOR and ESEEM effects and to illustrate their advantages and limitations by reference to recent applications.

The present chapter is structured as follows. In §2 the most important terms of the spin Hamiltonian are introduced and the relevant properties of nuclear fre-

quency spectra are discussed. The concept of orientation selection, which is of particular importance in disordered systems in EPR, is also presented. Section 3 gives an overview of experiments based on the ESEEM effect, starting with a short description of the origin of the nuclear modulation effect. After introducing the basic two- and three-pulse experiments in one dimension, special attention is paid to high-resolution two-dimensional methods such as hyperfine sublevel correlation spectroscopy (HYSCORE), as well as to special detection schemes for eliminating spectral artifacts. The concept of sensitivity enhancement using matched m.w. pulses is described and specific techniques developed in order to separate interactions from each other, i.e., hyperfine decoupling, are presented. Section 4 gives an overview of pulse ENDOR experiments. A brief introduction to the standard Davies and Mims ENDOR sequences is given. We then present a description of a selection of 2D experiments, as well as methods aimed at determining the sign or relative sign of the hyperfine interaction. A brief discussion of high-field ENDOR, resolution and sensitivity, and the hyperfine enhancement effect is presented. In §5, 2D field-swept EPR techniques for unraveling different interactions that contribute to a complex EPR lineshape are discussed (nutation experiments and electron Zeeman-resolved EPR).

2. SPIN HAMILTONIAN

This section gives an explanation of the different terms of the static spin Hamiltonian. The concept of orientation selection by selective m.w. excitation, which is central to many pulse EPR experiments on disordered systems, is explained.

2.1. Static Spin Hamiltonian

The static spin Hamiltonian is used to describe the energies of states of a paramagnetic species in the ground state with an effective electron spin S and m nuclei with spins I.

$$\mathcal{H}_0 = \mathcal{H}_{\mathrm{EZ}} + \mathcal{H}_{\mathrm{ZFS}} + \mathcal{H}_{\mathrm{HF}} + \mathcal{H}_{\mathrm{NZ}} + \mathcal{H}_{\mathrm{NQ}} \tag{1a}$$

$$= \beta_e \tilde{\mathbf{B}}_0 \mathbf{g} \mathbf{S} / \hbar + \tilde{\mathbf{S}} \mathbf{D} \mathbf{S} + \sum_{k=1}^{m} \tilde{\mathbf{S}} \mathbf{A}_k \mathbf{I}_k - \beta_n \sum_{k=1}^{m} g_{n,k} \tilde{\mathbf{B}}_0 \mathbf{I}_k / \hbar + \sum_{I_k > 1/2} \tilde{\mathbf{I}}_k \mathbf{P}_k \mathbf{I}_k \ . \tag{1b}$$

In this review all interactions are given in angular frequency units unless stated otherwise. $\mathcal{H}_0$ is called the spin Hamiltonian since it contains only phenomenological constants and spin coordinates described by the electron spin vector operator $\tilde{\mathbf{S}} = [\hat{S}_x, \hat{S}_y, \hat{S}_z]$ and the nuclear spin vector operators $\tilde{\mathbf{I}}_k = [\hat{I}_{x,k}, \hat{I}_{y,k}, \hat{I}_{z,k}]$. $\mathbf{B}_0$ is a vector describing the direction and strength of the permanent magnetic field. The transpose is denoted with a tilde. The terms describe: $\mathcal{H}_{\mathrm{EZ}}$, electron Zeeman interaction; $\mathcal{H}_{\mathrm{ZFS}}$, zero-field splitting; $\mathcal{H}_{\mathrm{HF}}$, hyperfine interactions between the electron

spins and m nuclear spins; $\mathcal{H}_{\mathrm{NZ}}$, nuclear Zeeman interactions; $\mathcal{H}_{\mathrm{NQ}}$, nuclear quadrupole interactions for $I > ½$. Equation (1) ignores high-order electron spin operators, and the spin–spin interactions between pairs of nuclear spins since its magnitude is very small compared to the other terms and the usual linewidths observed in paramagnetic complexes.

The information obtained from the spin Hamiltonian, the 3×3 matrices **g**, **D**, **A**, and **P**, is very sensitive to the geometric and electronic structure of the paramagnetic center. The electron Zeeman interaction reveals information about the electronic states; the zero-field splitting describes the coupling between electrons for systems where $S > ½$; the hyperfine interactions contain information about the spin density distribution [8] and can be used to evaluate the distance and orientation between the unpaired electron and the nucleus; the nuclear Zeeman interaction identifies the nucleus; the nuclear quadrupole interaction is sensitive to the electric field gradient at the site of the nucleus and thus provides information on the local electron density.

The hyperfine interaction is a key source of information on the spin density distribution. It can be written as the sum of the isotropic interaction or Fermi contact interaction $\mathcal{H}_{\mathrm{F}}$ and the electron-nuclear dipole–dipole coupling $\mathcal{H}_{\mathrm{DD}}$:

$$\mathcal{H}_{\mathrm{HF}} = \mathcal{H}_{\mathrm{F}} + \mathcal{H}_{\mathrm{DD}} = a_{\mathrm{iso}}\tilde{\mathbf{S}}\mathbf{I} + \tilde{\mathbf{S}}\mathbf{T}\mathbf{I}\,. \tag{2}$$

Here a_{iso} is the isotropic hyperfine coupling constant that is directly related to $|\psi_{\mathrm{o}}(0)|^2$, the electron spin density at the nucleus:

$$a_{\mathrm{iso}} = \frac{2\mu_0}{3\hbar} g_e \beta_e g_n \beta_n \left|\psi_o(0)\right|^2 . \tag{3}$$

Often a_{iso} is used to estimate the s-orbital spin population on the corresponding nucleus [9] (see, e.g., [10]). In Eq. (2) matrix **T** describes the anisotropic dipole–dipole coupling. The dominant contribution to $\mathcal{H}_{\mathrm{DD}}$, for nuclei other than protons, usually comes from the interaction of an electron spin in a p-, d-, or f-type orbital with the magnetic moment of the corresponding nucleus. By reference to suitable tables the dipole–dipole coupling can also be used to estimate the spin population in these orbitals [10]. For distances r_{k} between the electron and nuclear spin greater than approximately 0.25 nm, the anisotropic part of the hyperfine interaction can be used to calculate the electron–nuclear distance and orientation with the electron–nuclear point–dipole formula:

$$\mathbf{T} = \frac{\mu_0}{4\pi\hbar} g_e \beta_e g_n \beta_n \sum_{k \neq N} \frac{\rho_k (3\tilde{\mathbf{n}}_{\mathrm{k}}\mathbf{n}_{\mathrm{k}} - \mathbf{1})}{r_{\mathrm{k}}^{\,3}}, \tag{4}$$

where the sum is over all nuclei with spin population ρ_{k} at distance r_{k} from the nucleus with the electron–nucleus unit vector $\mathbf{n}_{\mathrm{k}}$. For an axial interaction with positive g_{n}, $\mathbf{T} = [-T, -T, 2T]$. Equation (4) gives very accurate information on proton positions provided the spin density distribution is known. It is also worth noting

that in many transition metal complexes there is a substantial orbital magnetic moment that adds pseudo-isotropic and pseudo-anisotropic contributions, and can be taken into account with $\mathbf{A} = a_{\mathrm{iso}}\mathbf{1} + \mathbf{gT}/g_e$ [11,12]. For systems with large g and/or T anisotropy this contribution to **A** cannot be neglected and needs to be included, particularly when analyzing high-resolution experiments like HYSCORE.

The spin Hamiltonian parameters of a complex or a model system can in principle be determined from a quantum chemical calculation of the electronic structure. The Density Functional Theory (DFT) [13] method is at present popular for this purpose, since it allows fairly large systems (~200 atoms) to be investigated. By comparing the calculated and experimental spin Hamiltonian parameters it is often possible to distinguish between different proposed models and to gain further insight into the electronic and geometric structure of the sample.

2.2. Nuclear Frequency Spectra of Spin Systems with $S = ½$ and Arbitrary I

Under the assumption $\mathcal{H}_{\mathrm{EZ}} \gg \mathcal{H}_{\mathrm{HF}} \gg \mathcal{H}_{\mathrm{NQ}}$, the first-order nuclear frequencies ($\omega^{(1)}$) for a nuclear spin I and an arbitrary orientation of the $\mathbf{B}_0$ field are given by

$$\omega^{(1)}(m_s, m_I \leftrightarrow m_I + 1) = c(m_s) + \tfrac{3}{2} P'_{zz}(m_s)(2m_I + 1)\,, \tag{5}$$

where

$$c(m_s) = \sqrt{\tilde{\mathbf{n}}\left(m_s \frac{\mathbf{gA}}{g} + \omega_I \mathbf{1}\right)\left(m_s \frac{\widetilde{\mathbf{gA}}}{g} + \omega_I \mathbf{1}\right)\mathbf{n}}\,, \tag{6}$$

and

$$P'_{zz}(m_s) = \frac{1}{c(m_s)^2}\tilde{\mathbf{n}}\left(m_s \frac{\mathbf{gA}}{g} + \omega_I \mathbf{1}\right)\mathbf{P}\left(m_s \frac{\widetilde{\mathbf{gA}}}{g} + \omega_I \mathbf{1}\right)\mathbf{n}\,. \tag{7}$$

n is a unit vector describing the orientation of $\mathbf{B}_0$ in the molecular frame. For the special case when **g**, **A**, and **P** are coaxial and $\mathbf{B}_0$ is parallel to one of the principal values A_i, Eq. (5) reduces to

$$\omega^{(1)} = \left|\frac{A_i}{2} \pm \omega_I\right| \quad \text{for } I = ½, \tag{8a}$$

$$\omega^{(1)} = \left|\frac{A_i}{2} \pm \omega_I \pm \frac{3}{2}P_i\right| \quad \text{for } I = 1, \tag{8b}$$

$$\omega^{(1)} = \left|\frac{A_i}{2} \pm \omega_I \pm \frac{3}{2}P_i(2m_I + 1)\right| \quad \text{for } I > 1. \tag{8c}$$

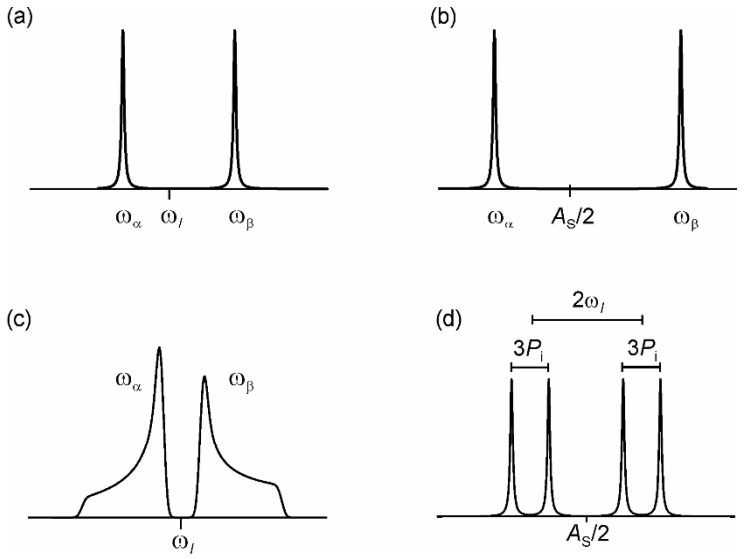

Figure 1. Typical nuclear frequency spectra for an $S = ½$ spin system with one nuclear spin: (a) single-crystal, $I = ½$, $2|\omega_I| > |A_S|$, $\omega_I < 0$, $A_S > 0$; (b) single crystal, $2|\omega_I| < |A_S|$; (c) powder spectrum for an axial hyperfine interaction; (d) single crystal, $I = 1$ with $\mathbf{B}_0$ along a principal axis. Modified with permission from [7]. Copyright © 2001, Oxford University Press.

For an $I = ½$ spin system Eq. (8a) shows that there are two frequencies symmetrically centered around $|\omega_I|$ (weak coupling case; $2|\omega_I| < |A_i|$) or $A_i/2$ (strong coupling case; $2|\omega_I| > |A_i|$). If the hyperfine interaction is anisotropic and $\mathbf{B}_0$ is not along one of the principal values, then the peaks are shifted to higher frequencies as, shown in Figure 1a,b. This shift is exploited in 2D techniques like HYSCORE. For nuclear spin $I > ½$, there is an additional splitting of the lines due to the nuclear quadrupole interaction (Fig. 1d).

The energy level diagram for an $S = ½$, $I = 1$ spin system is shown in Figure 2, and has four single-quantum (SQ) NMR transitions and two double-quantum (DQ) NMR transitions. In ENDOR spectroscopy, usually only the SQ transitions are observed; in ESEEM experiments both SQ and DQ transitions can be observed.

2.3. Orientation Selection in Pulse EPR

A resonator can be considered as a bandpass filter. The excitation bandwidth $\Delta\nu$ is determined by the resonator quality factor Q_L and is given by $Q_L = \nu/\Delta\nu$. For example, at X-band with $\nu = 9.8$ GHz and $Q_L = 100$, a total bandwidth of approximately 100 MHz or 3.5 mT is excited. In addition to the resonator, the excitation width of the m.w. pulse needs to be considered. With the maximum available microwave power and Q_L value the B_1 field strength is such that a $\pi/2$-pulse requires typically ~10 ns (a rectangular pulse of width L has a sinc function in the frequency domain with a full width at half height of $\cong 3.79/(2\pi L)$ Hz).

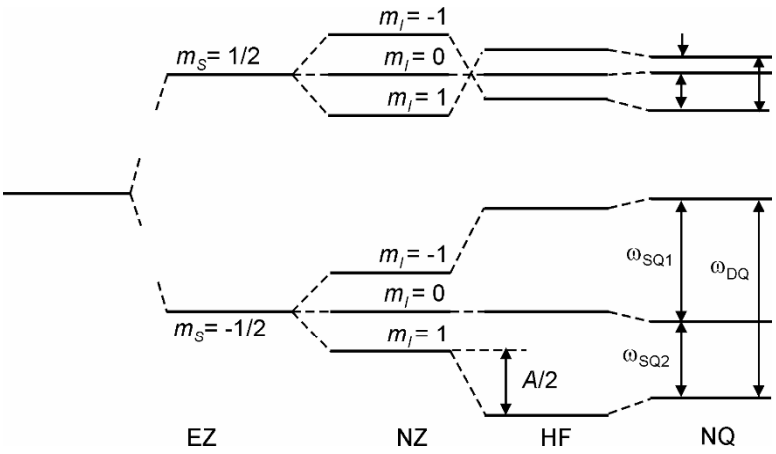

Figure 2. Energy level diagram for an $S = ½$, $I = 1$ spin system in the strong coupling case, $2|\omega_I| < |A_S|$.

The resulting excitation bandwidth may be enough to excite the complete spectrum of an organic radical at X-band, but typically only excites a narrow region of the spectrum from a transition metal complex. Consider for example the EPR spectrum of Cob(II)alamin with *g*-values of $g_1 = 2.272$, $g_2 = 2.230$, $g_3 = 2.004$ [14]. At X-band the EPR spectrum has a width of 90 mT (~2 GHz), and at W-band it is 400 mT (~11 GHz) wide. The effective excitation bandwidth of the pulse, in comparison to the EPR spectrum, thus provides orientation selection in disordered samples. This orientationally selective excitation allows the magnetic interactions, with respect to the *g*-matrix coordinate system, to be estimated.

Figure 3a shows a calculated EPR spectrum for a rhombic *g*-matrix (the *g*-values correspond to the so called "red2" signals from methyl coenzyme reductase) [15]. For a pulse experiment (e.g., ENDOR or HYSCORE) preformed at the field position corresponding to g_1, only molecules with their g_1 axis ($\mathbf{g}_1$) oriented along or close to $\mathbf{B}_0$ contribute to the experiment. At the high-field end at the observer position corresponding to g_3, only molecules with $\mathbf{g}_3$ oriented close to or along $\mathbf{B}_0$ contribute to the experiment. These positions, at the extreme high- and low-field ends of the EPR spectrum, are referred to as "single-crystal" like. With $\mathbf{B}_0$ at the observer position corresponding to the g_2 value, many orientations of the paramagnetic center are resonant with the m.w. pulse and contribute to the experiment. Figure 3b,c shows a calculation for Cob(II)alamin at X-band and Q-band, respectively. At X-band, the orientation selection for experiments performed at the field positions corresponding to g_1 and g_2 are particularly poor since the small *g*-anisotropy and large cobalt hyperfine interaction result in many orientations contributing to the experiment. At Q-band the situation is much improved and two "single-crystal" like positions are possible at the low- and high-field ends.

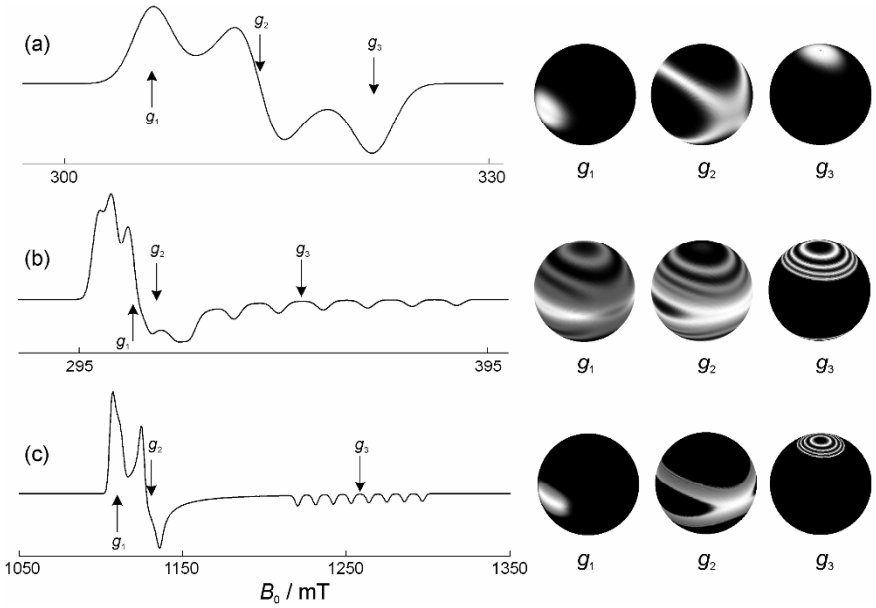

Figure 3. Calculated EPR spectra and orientation selection on the unit sphere for the observer ($\mathbf{B}_0$ field) positions corresponding to g_1, g_2, and g_3. White indicates orientations on-resonance with the m.w. pulse, black shading is off-resonance. The m.w. pulse for the orientation selection has a width of 25 MHz. (a) Orthorhombic spectrum of MCR_{red2}[15] at X-band (9.8 GHz) with g-values of $g_1 = 2.287$, $g_2 = 2.231$, $g_3 = 2.175$, and a linewidth of 100 MHz. (b) spectrum of Cob(II)alamin[14] with $g_1 = 2.272$, $g_2 = 2.230$, $g_3 = 2.004$, cobalt ($I = 7/2$) hyperfine couplings $A_1 = 30$ MHz, $A_2 = 40$ MHz, $A_3 = 305$ MHz, and a linewidth of 50 MHz. (c) same as in (b) but at Q-band (35.3 GHz).

3. ESEEM BASICS

3.1. Origin of the Nuclear Modulation Effect

The nuclear modulation effect was first observed by Rowan, Hahn, and Mims [16], and the theory was later developed by Mims in 1972 [17]. The origin of the nuclear modulation effect can be understood with a semi-quantitative discussion using a two-spin model system consisting of one electron spin ($S = ½$) and one nuclear spin ($I = ½$). Assuming an isotropic g-matrix and an anisotropic hyperfine interaction, the spin Hamiltonian in the rotating frame can be written as

$$\mathcal{H}_0 = \Omega_S S_z + \omega_I I_z + A S_z I_z + B S_z I_x , \tag{9}$$

where $\Omega_S = \omega_S - \omega_{mw}$ is the resonance offset of the electron Zeeman frequency ($\omega_s = g\beta_e B_0 / \hbar$) from the m.w. frequency ω_{mw}, and A, B describe the secular and

pseudo-secular part of the hyperfine coupling. In the case of an axially symmetric hyperfine interaction, A and B are given by

$$A = a_{\text{iso}} + T(3\cos^2\theta - 1), \quad B = 3T\sin\theta\cos\theta. \tag{10}$$

T and a_{iso} are the dipolar and the isotropic hyperfine coupling and θ is the angle between the electron–nuclear vector and the external static magnetic field $\mathbf{B}_0$.

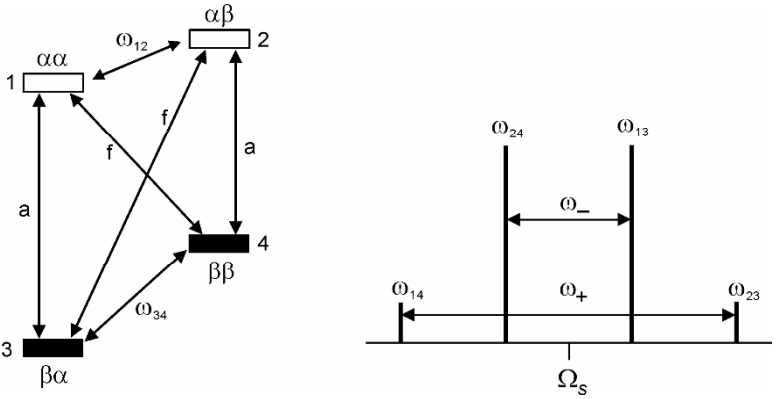

Figure 4. Energy level diagram (left) and corresponding schematic EPR spectrum (right) for an $S = ½$, $I = ½$ model system with $|A_S| < |2\omega_I|$ (weak-coupling case): **a:** allowed EPR transitions (1,3) and (2,4); **f**: forbidden EPR transitions (1,4) and (2,3); nuclear transitions (1,2) and (3,4). Modified with permission from [7]. Copyright © 2001, Oxford University Press.

In this four-level system, shown in Figure 4, there are two allowed ($\Delta m_S = \pm 1$, $\Delta m_I = 0$) and two forbidden ($\Delta m_S = \pm 1$, $\Delta m_I = \pm 1$) EPR transitions with frequencies given by

$$\begin{aligned}
\omega_{13} &= \omega_S + \omega_-/2, \\
\omega_{24} &= \omega_S - \omega_-/2, \\
\omega_{14} &= \omega_S + \omega_+/2, \\
\omega_{23} &= \omega_S - \omega_+/2,
\end{aligned} \tag{11}$$

with $\omega_+ = \omega_\alpha + \omega_\beta$, $\omega_- = \omega_\alpha - \omega_\beta$, and the nuclear frequencies ω_α and ω_β corresponding to the two NMR transitions being given by

$$\omega_\alpha = |\omega_{12}| = \left[\left(\omega_I + \frac{A}{2}\right)^2 + \left(\frac{B}{2}\right)^2\right]^{1/2}, \quad \omega_\beta = |\omega_{34}| = \left[\left(\omega_I - \frac{A}{2}\right)^2 + \left(\frac{B}{2}\right)^2\right]^{1/2}. \tag{12}$$

The transition probabilities of the allowed (I_a) and forbidden (I_f) EPR transitions are given by Eq. (13), where 2η is the angle between the nuclear quantization axes in the two m_S manifolds with respect to $\mathbf{B}_0$ [7]:

$$I_a = \cos^2\eta = \frac{\left|\omega_I^2 - \frac{1}{4}\omega_-^2\right|}{\omega_\alpha\omega_\beta}, \quad I_f = \sin^2\eta = \frac{\left|\omega_I^2 - \frac{1}{4}\omega_+^2\right|}{\omega_\alpha\omega_\beta}. \tag{13}$$

For the isotropic coupling case ($T = 0$) the B term vanishes and $I_a = 1$, $I_f = 0$. Then the EPR stick spectrum (Fig. 4, right) consists of only two lines corresponding to the allowed transitions split by $\omega_- = a_{iso}$. The addition of an anisotropic part to the hyperfine coupling ($T \neq 0$) mixes the energy levels so that they are no longer pure α or β with respect to the nuclear spin state. This in turn results in a nonzero probability for the forbidden EPR transitions, which provides the basis of the ESEEM effect.

3.2. Two- and Three-Pulse ESEEM

In the two-pulse ESEEM experiment (Fig. 5a), the intensity of the primary echo is recorded as a function of the time interval τ between the π/2 and π pulses. The modulation formula for an $S = ½$, $I = ½$ spin system is given by

$$V_{2p}(\tau) = 1 - \frac{k}{4}[2 - 2\cos(\omega_\alpha\tau) - 2\cos(\omega_\beta\tau) + \cos(\omega_-\tau) + \cos(\omega_+\tau)], \tag{14}$$

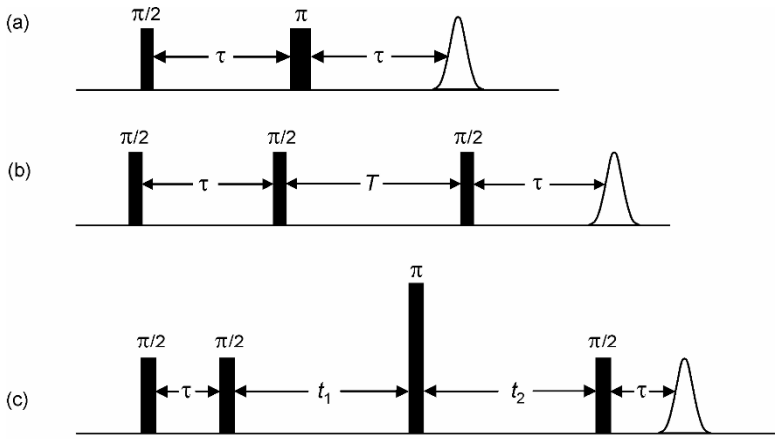

Figure 5. Pulse sequences making use of the ESEEM effect. (a) Two-pulse sequence and the primary echo. (b) Three-pulse sequence and the stimulated echo. (c) Four-pulse sequence for the HYSCORE experiment.

where k is the orientation-dependent modulation depth parameter given by

$$k(\theta) = \left(\frac{B\omega_I}{\omega_\alpha \omega_\beta} \right)^2 \tag{15}$$

For the case of an isotropic hyperfine interaction $\mathbf{A}=a_{\mathrm{iso}}\mathbf{I}$, or if $\mathbf{B}_0$ is oriented along one of the principal axes of the hyperfine tensor ($\theta = 0$ or $\theta = \pi/2$), the echo modulation disappears, since in either of these cases the quantity B in Eq. (15) becomes zero.

Equation 14 consists of an unmodulated part with amplitude $1 - k/2$, the basic frequencies ω_α and ω_β with amplitudes $k/2$, and the combination frequencies ω_- and ω_+ with amplitudes $k/4$, and inverted phase. To compute the frequency-domain spectrum, first the unmodulated part is subtracted, as it gives a dominant peak at zero frequency for the usual case of small k values. A cosine Fourier transform (FT) of the time trace results in a spectrum that contains the two nuclear frequencies, ω_α and ω_β, with positive intensity, and their sum and difference frequencies, ω_+ and ω_-, with negative intensity. If the initial part of the time-domain trace is missing, then the spectrum can be severely distorted by frequency-dependent phase shifts and it may be best to FT the time-domain trace and compute the magnitude spectrum.

In multinuclear spin systems the echo modulation is given by the product rule [17]:

$$V_{2\mathrm{p}}(\tau) = \prod_i^N V_{2\mathrm{p}}^i(\tau), \tag{16}$$

where $V_{2\mathrm{p}}^i(\tau)$ is given by Eq. (14) and N is the number of nuclei coupled to the electron spin. In this case the spectrum contains, in addition to the four basic frequencies, combination frequencies. Combination frequencies arise from the sum or difference of nuclear frequencies from different nuclei of the same paramagnetic center. The simple form of Eq. (16) can be used to identify modulations originating from specific nuclei. This can be achieved by dividing the time traces from two samples, one before and one after isotopic substitution of the nucleus of interest. As a consequence of the product rule, all modulation components that are common to the two samples vanish when the ratios of the two ESEEM time traces are calculated [18,19].

The main shortcoming of the two-pulse experiment is that the primary echo decays within the phase memory time, T_{M}, which is often very short. This can prevent the observation of low-frequency modulations, and thus the estimation of the magnetic parameters can become uncertain. Another important limitation arises from the spectrometer deadtime τ_{d} (typically 100–150 ns at X-band frequencies), which restricts the observation of the signal to times $t > \tau_{\mathrm{d}}$. The loss of the initial part of the time trace can cause severe distortions in the frequency-domain spectrum, especially in disordered systems where destructive interference from differ-

ent resonance frequencies is more pronounced. The initial part of the time trace can be recovered by employing a remote-echo detection scheme (see §3.4).

The disadvantage of the fast echo decay in two-pulse ESEEM can be circumvented with the three-pulse ESEEM experiment shown in Figure 5b. In this pulse sequence the first two π/2 pulses create nuclear coherence that develops during the evolution time T and decays with the transverse nuclear relaxation time T_{2n}, which is usually much longer than the corresponding relaxation time T_M of the electrons. The third π/2 pulse transfers the nuclear coherence back to observable electron coherence. The modulation of the stimulated echo is given by

$$V_{3p}(\tau,T) = \tfrac{1}{2}[V^{\alpha}(\tau,T) + V^{\beta}(\tau,T)], \tag{17a}$$

with the contribution from the α electron spin manifold

$$V^{\alpha}(\tau,T) = 1 - \frac{k}{2}[1-\cos(\omega_{\beta}\tau)][1-\cos(\omega_{\alpha}(\tau+T))], \tag{17b}$$

and an analogous expression for $V^{\beta}(\tau,T)$:

$$V^{\beta}(\tau,T) = 1 - \frac{k}{2}[1-\cos(\omega_{\alpha}\tau)][1-\cos(\omega_{\beta}(\tau+T))]. \tag{17c}$$

It is worth reiterating that nuclear coherence, comprising nuclear frequencies of the spin system, is created by the first two m.w. pulses. During evolution time T the nuclear coherence accumulates phase, and the transfer of this nuclear coherence back to electron coherence with the third m.w. pulse causes the stimulated echo intensity to be modulated by the nuclear frequencies, enabling their measurement.

When T is varied the echo envelope is modulated only by the two basic frequencies ω_{α} and ω_{β}, the sum and difference frequencies do not appear, in contrast to the two-pulse ESEEM experiment. This is usually advantageous, as it simplifies spectra, but it may also be a disadvantage for disordered systems where the sum-combination line is often the only narrow feature in the ESEEM spectrum. Another important difference is the dependence of the three-pulse ESEEM amplitudes on τ, as is apparent from Eq. (17) by the factors $1 - \cos(\omega_{\beta}\tau)$ and $1 - \cos(\omega_{\alpha}\tau)$. Due to this suppression effect, individual peaks in the spectrum can disappear completely. These blind spots occur for the α(β) peak when $\tau = 2\pi n/\omega_{\beta(\alpha)}$ (n = 1, 2, …). In principle they can be avoided by using $\tau < 2\pi/\omega_{max}$, where ω_{max} is the maximum nuclear frequency; however, this is usually precluded by the spectrometer deadtime. Consequently, the three-pulse ESEEM experiment has to be performed at several τ values to avoid misinterpretation of the spectra due to blind-spot artifacts.

For several nuclear spins the product rule gives [20]

$$V_{3p}(\tau,T) = \frac{1}{2}\left[\prod_{l=1}^{N} V_l^{\alpha}(\tau,T) + \prod_{l=1}^{N} V_l^{\beta}(\tau,T)\right]. \tag{18}$$

As a consequence of Eq. (18), combinations of the nuclear frequencies occur only within the same electron spin manifold, in contrast to the two-pulse experiment. This allows the relative sign of two hyperfine couplings to be determined if combination peaks are observed [14]. Another consequence of the product rule is an effect where nuclei with deep modulations partially or completely suppress signals from nuclei with shallow modulations [21]. For example, a ^{14}N nucleus close to the cancellation regime at X-band will have a large modulation depth, and can completely suppress weaker ^{1}H or ^{19}F signals. This additional suppression effect has a serious impact on spectral intensities and can lead to misinterpretation of spectral features, for instance, when spectra from a compound in nondeuterated and deuterated solvents are compared. Such experiments are often used to identify exchangeable protons by the disappearance or reduction in intensity of certain ^{1}H lines [22]. However, deuterons with deep modulations can suppress all ^{1}H peaks. Due care therefore has to be exercised when three-pulse ESEEM spectra are compared.

The suppression effects mentioned above are inherent in the spin dynamics of ESEEM experiments using the nuclear coherence generator $\pi/2 - \tau - \pi/2$. Therefore, they cannot be completely eliminated by any choice of experimental parameters. Techniques for minimizing the suppression effects are discussed in §3.4.

3.3. HYSCORE

In powder samples or frozen solutions the modulation pattern usually decays very much faster than the overall amplitude of the echo, owing to the destructive interference of the different resonance frequencies. Consequently, the advantage of slow echo decay in three-pulse ESEEM cannot be fully utilized for disordered systems. This problem can be solved with the four-pulse sequence shown in Figure 5c, where an additional π pulse is introduced between the second and third $\pi/2$ pulse of the three-pulse ESEEM experiment. During the first evolution period t_1, the nuclear coherence created by the $\pi/2 - \tau - \pi/2$ subsequence evolves in the $\alpha(\beta)$ electron spin manifold. The nonselective π pulse acts as a mixer that interchanges the nuclear coherence between the electron spin α and β manifolds. During the second evolution period t_2, the transferred nuclear coherence evolves in the $\beta(\alpha)$ electron spin manifold and a nuclear coherence transfer echo (CTE) is created at about $t_1 = t_2$ as a result of the refocusing of the hyperfine anisotropy [23]. Finally, the nuclear coherences are transferred to electron coherence by the last $\pi/2$ pulse and are detected as an electron spin echo, which is modulated by the nuclear frequencies. The observation of the nuclear CTE allows one to measure the in-phase part of the modulation and its decay with respect to both t_1 and t_2. This is an important advantage as compared to the three-pulse ESEEM experiment, since the spectrum consists of undistorted absorption peaks.

Three different 1D ESEEM schemes using the pulse sequence in Figure 5c and the nuclear CTE have been proposed; deadtime-free ESEEM by nuclear coherence transfer echoes (DEFENCE) [24], the combination peak (CP) experiment, and the

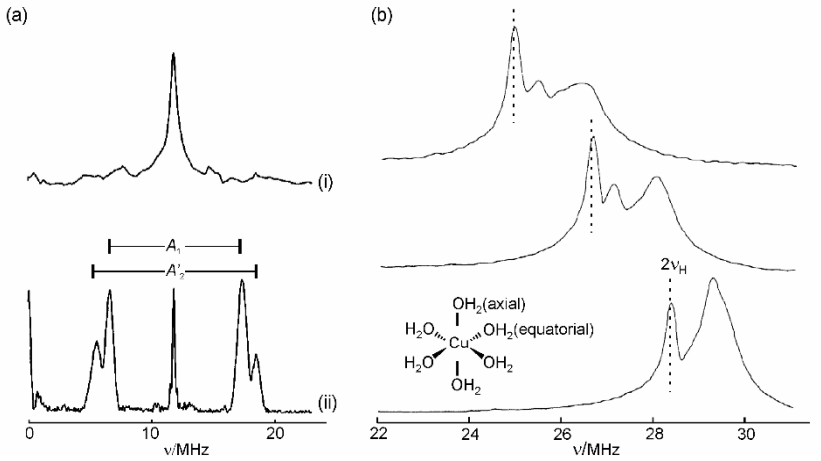

Figure 6. Examples of 1D four-pulse ESEEM experiments. (a) Comparison of three-pulse ESEEM (i) and DEFENCE (ii) experiments of bis(η^6-benzene)vanadium(0), $V(C_6H_6)_2$, diluted into polycrystalline ferrocene; observer position, $g_\perp$. (b) Combination-peak spectra of $[Cu(H_2O)_6]^{2+}$ centers in a frozen water/glycerol solution measured at three different observer positions. The dashed lines mark the frequency $2\nu_H$. Modified with permission from [24] and [26]. Copyright © 1995, American Institute of Physics.

hyperfine (HF) spectroscopy experiment [25]. The DEFENCE experiment, where the time interval t_1 is fixed and t_2 is swept, gives undistorted 1D ESEEM spectra that contain the nuclear frequencies ω_α and ω_β. This is demonstrated in Figure 6a, which compares the absolute-value spectra from DEFENCE and a three-pulse ESEEM experiment on bis(η^6-benzene)vanadium(0), $V(C_6H_6)_2$, diluted into polycrystalline ferrocene. The three-pulse ESEEM spectrum is dominated by a broad and featureless matrix peak, and signals from the benzene ring protons are hardly recognizable. The resolution is drastically improved in the DEFENCE spectrum, from which one can readily read out the hyperfine couplings $A_1 = 9.2$ MHz and $A_2' = 14.4$ MHz that correspond to the extremes of the proton hyperfine couplings in the benzene ring plane.

In the CP experiment, times t_1 and t_2 are incremented under the constraints $t_1 = t_{10} + t$, $t_2 = t_{20} + t$, enabling the combination frequencies $\omega_+ = \omega_\alpha + \omega_\beta$ to be measured. This is very helpful in studies of disordered systems, where the peaks of the nuclear frequencies are often broad and difficult to observe. The combination peaks appear as narrow features in the spectrum since the orientation-dependent hyperfine interactions are partially refocused. For weak hyperfine couplings with $|B| \pm |\omega_I \pm A/2|$, the maximum of the sum-combination frequency is given by

$$(\omega_+)_{\max} = 2|\omega_I| + \frac{9}{16}\frac{T^2}{|\omega_I|}, \tag{19}$$

so that T can be inferred. CP experiments are particularly useful for assigning proton hyperfine couplings. Figure 6b shows combination-peak spectra of $[Cu(H_2O)_6]^{2+}$ centers in frozen solution measured at different B_0 field positions [26]. Depending on the selected orientation, the spectra consist of two or three combination-frequency peaks. The peak at $2\nu_H$ arises from weakly coupled protons of the solvent molecules. The broad line with a frequency shift Δ of 1.2–1.5 MHz results from the protons of water molecules coordinated in the equatorial plane, whereas the peaks with $\Delta \approx 0.5$ MHz are assigned to axial water protons. A recent study of low-spin ferric complexes using 1D–CP experiments at different observer positions allowed the dipolar parts of the hyperfine interactions of the nearest protons of the axially coordinated imidazole ligands to be determined [27].

In the HF experiment, times t_1 and t_2 are incremented under the constraints $t_1 = t_{10} + t$, $t_2 = t_{20} - t$, with $t_1 + t_2 = t_{10} + t_{20} = T_0 = \text{const}$ (see Fig. 5c). The total accumulated phase of the nuclear coherence is given by $(\omega_{12} - \omega_{34})t + \omega_{12}t_{10} + \omega_{34}t_{20}$. Since time t is varied and t_{10} and t_{20} are kept constant, the echo is modulated with the frequency $|\omega_-| = |\omega_\alpha - \omega_\beta|$, which, for the weak coupling case, becomes $|\omega_-| = |A_S|$. Therefore, despite some peculiarities [25], this experiment allows for the measurement of undistorted hyperfine spectra.

The 1D methods described above result in undistorted ESEEM spectra and thus can drastically improve resolution. However, in multinuclear spin systems having strongly coupled nuclei with small gyromagnetic ratios and weakly coupled nuclei with large gyromagnetic ratios, peaks may overlap and the spectrum can be complicated and difficult to analyze. The resolution can be further increased by implementing the HYSCORE experiment where times t_1 and t_2 are incremented independently [28]. As a consequence of the transfer of nuclear coherence by the π pulse, this 2D experiment correlates nuclear frequencies from different m_S manifolds. For an $S = ½$, $I = ½$ spin system and ideal pulses the modulation formula for the HYSCORE experiment can be written as [29]

$$V_{4p}(\tau,t_1,t_2) = \tfrac{1}{2}[V^{\alpha\beta}(\tau,t_1,t_2) + V^{\beta\alpha}(\tau,t_1,t_2)], \tag{20}$$

with the terms

$$\begin{aligned} V^{\alpha\beta}(\tau,t_1,t_2) &= 1 - \frac{k}{2}\left\{\frac{C_0}{2} + C_\alpha \cos\left[\omega_{12}\left(t_1 + \frac{\tau}{2}\right)\right] + C_\beta \cos\left[\omega_{34}\left(t_2 + \frac{\tau}{2}\right)\right]\right. \\ &\left. + C_c\left[\cos^2\eta\cos\left(\omega_{12}t_1 + \omega_{34}t_2 + \omega_+\frac{\tau}{2}\right) - \sin^2\eta\cos\left(\omega_{12}t_1 - \omega_{34}t_2 + \omega_-\frac{\tau}{2}\right)\right]\right\} \\ V^{\beta\alpha}(\tau,t_1,t_2) &= 1 - \frac{k}{2}\left\{\frac{C_0}{2} + C_\alpha \cos\left[\omega_{12}\left(t_2 + \frac{\tau}{2}\right)\right] + C_\beta \cos\left[\omega_{34}\left(t_1 + \frac{\tau}{2}\right)\right]\right. \\ &\left. + C_c\left[\cos^2\eta\cos\left(\omega_{34}t_1 + \omega_{12}t_2 + \omega_+\frac{\tau}{2}\right) - \sin^2\eta\cos\left(\omega_{34}t_1 - \omega_{12}t_2 - \omega_-\frac{\tau}{2}\right)\right]\right\} \end{aligned} \tag{21}$$

and the coefficients

$$\begin{aligned} C_0 &= 3-\cos(\omega_{12}\tau)-\cos(\omega_{34}\tau)-\sin^2\eta\cos(\omega_+\tau)-\cos^2\eta\cos(\omega_-\tau),\\ C_\alpha &= \cos^2\eta\cos((\omega_{34}-\omega_{12}/2)\tau)+\sin^2\eta\cos((\omega_{34}+\omega_{12}/2)\tau)-\cos(\omega_{12}\tau/2),\\ C_\beta &= \cos^2\eta\cos((\omega_{12}-\omega_{34}/2)\tau)+\sin^2\eta\cos((\omega_{12}+\omega_{34}/2)\tau)-\cos(\omega_{34}\tau/2),\\ C_c &= -2\sin(\omega_{12}\tau/2)\sin(\omega_{34}\tau/2). \end{aligned} \tag{22}$$

Three different kinds of peaks appear in the HYSCORE spectrum after the FT of the time-domain signal along both dimensions, as depicted in Figure 7. The first terms of Eq. (21) with coefficients C_α and C_β originate from the transfer of nuclear coherence to polarization (and vice versa) and lead to the axial peaks $(0,\omega_{12})$, $(0,\omega_{34})$ and $(\omega_{12},0)$, $(\omega_{34},0)$ (open circles). These peaks are usually not of interest and are typically removed by a baseline correction.

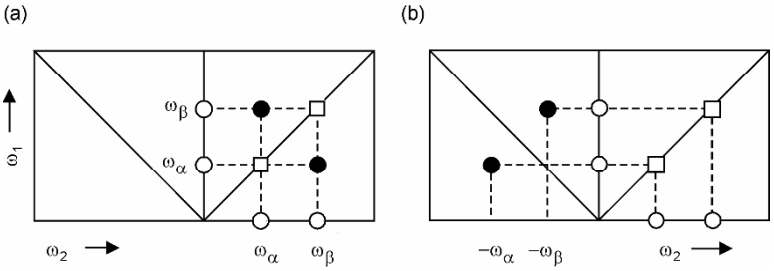

Figure 7. Peaks in HYSCORE spectra. Full circles represent the wanted cross-peaks, open circles represent axial peaks due to transfer of nuclear coherence to polarization, and vice versa, by the mixing π pulse. Open squares represent diagonal peaks caused by pulse non-ideality: (a) Weak-coupling case, $|A_S| < 2|\omega_I|$; and (b) Strong coupling case $|A_S| > 2|\omega_I|$. Modified with permission from [7]. Copyright © 2001, Oxford University Press.

The terms with the coefficient C_c arise from the interchange of nuclear coherences between the two m_S manifolds and give cross-peaks at $(\omega_{12},\omega_{34})$ and $(\omega_{34},\omega_{12})$ with the weighting factor $\cos^2\eta$ (full circles), and cross-peaks at $(\omega_{12},-\omega_{34})$ and $(\omega_{34},-\omega_{12})$ with the weighting factor $\sin^2\eta$ (not shown). For intermediate couplings, $2|\omega_I| \sim |A_S|$, the cross-peaks have comparable intensities in the first and second quadrants. For the very weak- or strong-coupling case, the weighting factor $\sin^2\eta$ is much smaller than $\cos^2\eta$ and, consequently, the cross-peaks at $(\omega_{12},\omega_{34})$ and $(\omega_{34},\omega_{12})$ dominate the spectrum (i.e., cross-peaks are observed in either the first (third) or the second (fourth) quadrant). For the weak-coupling case, where ω_{12} and ω_{34} have the same sign, the stronger cross-peaks are observed in the first (and third) quadrants (Fig. 7a). For the strong-coupling case ω_{12} and ω_{34} have opposite signs and the stronger cross-peaks appear in the second (and fourth) quadrant (Fig. 7b). This feature introduces additional spectral

information since peaks corresponding to weak and strong couplings are separated from each other and can thus be easily identified.

Apart from axial-peaks and cross-peaks, the diagonal-peaks (ω_{12},ω_{12}) and (ω_{34},ω_{34}) can also be present in the HYSCORE spectrum as a result of the incomplete transfer of nuclear coherence due to nonideality of the π pulse (see Fig. 7). Their intensity can be significantly reduced by using a larger excitation bandwidth for the mixing pulse (shorter pulse length) than for the $\pi/2$ pulses that generate and detect the nuclear coherence. Apart from the weighting factors $\cos^2\eta$ and $\sin^2\eta$, the intensities of the HYSCORE cross-peaks are also determined by two important parameters: the modulation depth k and the coefficient C_c. First, the intensities of the peaks at the canonical orientations vanish since here $k = 0$ [Eq. (15)], and, second, the term C_c induces blind spots at $\nu = n/\tau$ (n = 0, 1, 2, ...) in both dimensions [Eq. (22)].

The analysis of HYSCORE spectra by means of peak intensities is not a straightforward process. Deviations from the analytical formulas given in Eqs. (20)–(22) can occur due to nonideality of the pulses. In addition, for multinuclear spin systems and/or systems with $I > 1$, analytical solutions become tedious and physical insight is not easily acquired. In disordered systems the task becomes very demanding because orientation selection and additional amplitude effects due to destructive interferences [30] have to be taken into account. For these reasons, numerical simulations are very important for analyzing peak positions and intensities of HYSCORE spectra. Even though there is significant progress on the development of simulation programs [31,32], an accurate and general quantitative interpretation of peak intensities via numerical simulations has not yet been clearly established. Consequently, the information extracted from HYSCORE spectra is often based primarily on the analysis of peak positions.

Figure 8 shows typical HYSCORE powder patterns for an S = ½, I = ½ spin system. In the strong-coupling case, $|A_S| > 2|\omega_I|$, the correlation ridges orient parallel to the diagonal and are separated by $2|\omega_I|$ only at the orientations corresponding to the principal values. In the weak-coupling case, $|A_S| < 2|\omega_I|$, the two arcs are displaced from the antidiagonal at $|\omega_I|$, with a maximum frequency shift given by [33]

$$\Delta\omega_{max} = \frac{9}{32}\frac{T^2}{|\omega_I|}. \tag{23}$$

The advantage of $\Delta\omega_{max}$ for inferring the anisotropic part of the hyperfine interaction arises from the fact that the intensities of the endpoints of the arcs (corresponding to the principal values) vanish since here the depth parameter $k = 0$. Therefore, the hyperfine parameters cannot be determined easily from the extension of the ridges perpendicular to the diagonal. In addition to this approach, the lineshapes of ESEEM spectra for S = ½, I = ½ spin systems have been thoroughly studied [34], and useful representations of the correlation patterns in order to determine a_{iso} and T have been proposed [35].

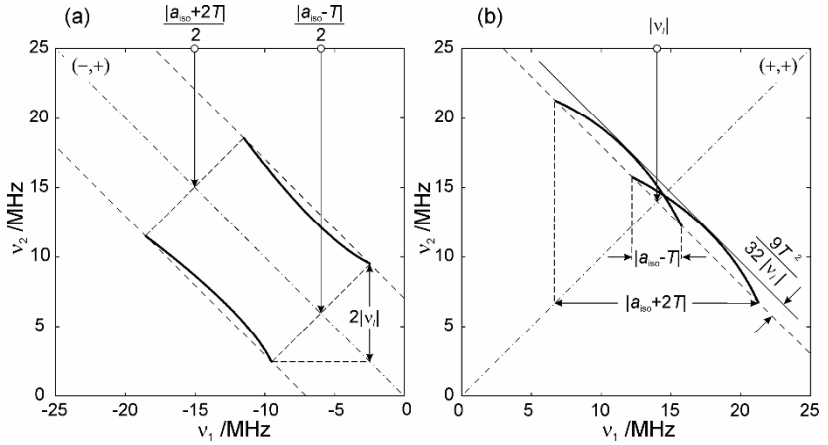

Figure 8. Theoretical HYSCORE powder patterns for an $S = ½$, $I = ½$ spin system with an axial hyperfine tensor. (a) Strong-coupling case with $\nu_I = 3.5$ MHz, $a_{iso} = 18$ MHz, and $T = 6$ MHz. (b) Weak-coupling case with $\nu_I = 14$ MHz, $a_{iso} = 2.5$ MHz, and $T = 6$ MHz.

Figure 9 shows ^{1}H and ^{13}C HYSCORE spectra from the complex MCR_{BPS} ($S = ½$, nickel-based EPR signal). MCR_{BPS} is a potent inhibitor of the enzyme methyl-coenzyme M reductase (MCR) [36] and results from reaction of $Ni^{I}F_{430}$ (active site of MCR) with 3-bromopropane sulfonate to give a bromide ion and $^{-}O_3S(CH_2)_3$–$Ni^{III}F_{430}$ in the active site (see figure) [37,38]. An Ni alkyl bond is thus formed.

The X-band proton HYSCORE spectrum (Fig. 9a) allows signals from the two H_γ protons that are bonded to the C_γ coordinated to the nickel to be resolved. Due to their close proximity to the main part of the spin density, located on the γ-carbon and nickel, the two proton hyperfine interactions have large anisotropies, $A(^1H_\gamma) \cong$ [–10,–1,14] MHz. This displaces the signals from the antidiagonal [Eq. (23)] and allows them to be resolved from the many other protons comprising the "matrix line." A second signal with a large isotropic hyperfine component could also be resolved and is assigned to $H_{\beta 1}$, $A(^1H_{\beta 1}) = [16.3, 8.0, 20.7]$ MHz. Figure 9b shows a Q-band ^{13}C HYSCORE spectrum measured near to the echo maximum. The appearance of ^{13}C signals in both quadrants indicates that for the many sample orientations contributing at this observer position the hyperfine couplings go from the weak to the strong coupling case ($2\nu_I = 25.5$ MHz). In the graph the principal values of the hyperfine interaction, $A(^{13}C) = [17.6, 18.3, 45.0]$ MHz, are indicated. These were determined from a set of HYSCORE and ENDOR data. From a biological perspective, the detection of this alkyl-nickel species in the active site of MCR adds plausibility to proposed mechanisms proceeding via such intermediates, and this new type of alkyl-nickel species detected by EPR could play a crucial role in the C–H activation step in MCR. For example, in one proposed mechanism the Ni(I) acts as a nucleophile attacking CH_3–S–CoM at the carbon of the CH_3–S group, generating a CH_3–Ni(III)F_{430} intermediate.

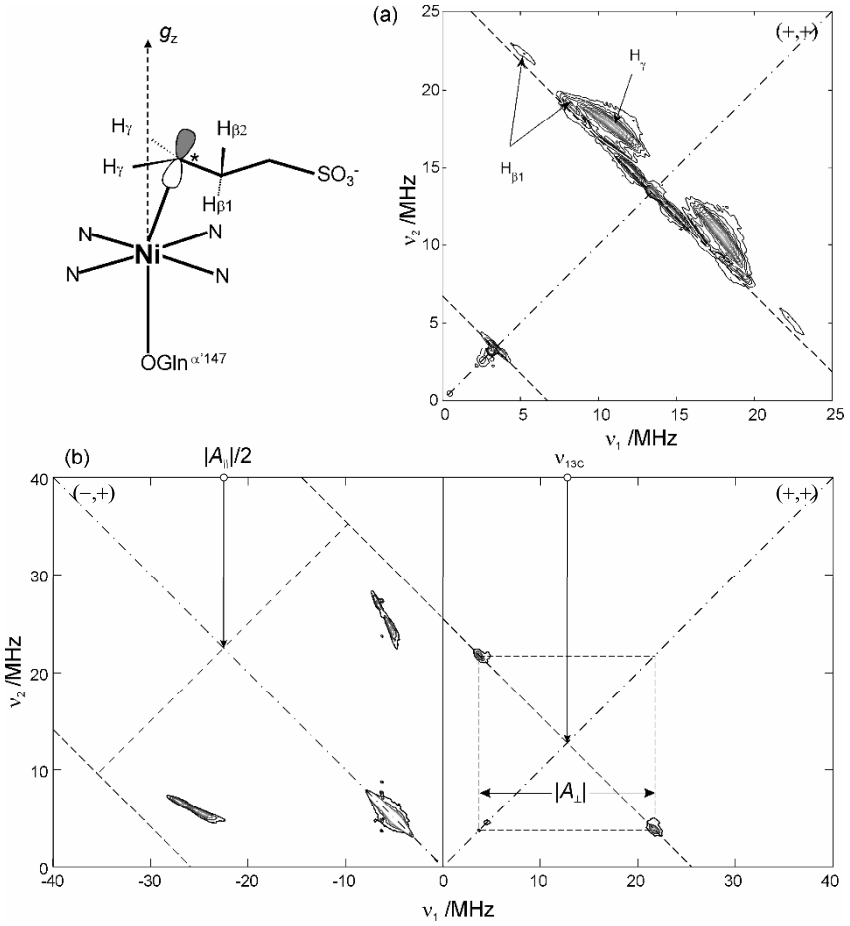

Figure 9. HYSCORE spectra of MCR_{BPS} (see schematic for structure). (a) ^1H X-band (9.7 GHz) spectrum at 20 K, with signals assigned to H_γ and $H_{\beta1}$. (b) ^{13}C Q-band (35.3 GHz) spectrum at 20 K. The position of the principal values, determined from the full set of HYSCORE and ENDOR spectra, are indicated. The intense signal on the diagonal around (–5,5) MHz is due to an incomplete transfer of nuclear coherences between the two electron spin manifolds by the non-ideal π pulse. Modified with permission from [38]. Copyright © 2006, Wiley-VCH.

For a nucleus with $I = 1$ and nonnegligible quadrupole coupling, e.g., ^{14}N, 18 correlation ridges are expected but typically not all of them are observed in the HYSCORE spectrum. This may be because of broadening due to hyperfine and quadrupole anisotropy, or low transition probabilities. The double-quantum transitions $(m_I, m_I + 2) = (–1,1)$ do not depend to first order on the nuclear quadrupole coupling [see Eq. (8b)], hence correlation patterns similar to those found for nuclei with $I = ½$ are expected. In contrast, the single-quantum transitions $(m_I, m_I+1) =$

(0,1) and (–1,0) depend to first order on the nuclear quadrupole coupling and, therefore, are usually broad in disordered systems. For this reason the most prominent features of ^{14}N HYSCORE spectra are often the double-quantum cross-peaks. The situation is different when the nuclear quadrupole interaction is much weaker than the nuclear Zeeman and hyperfine interaction, which is the usual case for deuterium bonded to carbon. Under these conditions the transition probabilities of the double-quantum transitions are very small and the single-quantum correlation peaks dominate the spectrum [39]. Analytical formulas describing the frequencies and shapes of the cross-peaks for $I = 1$ have also been derived [40,41].

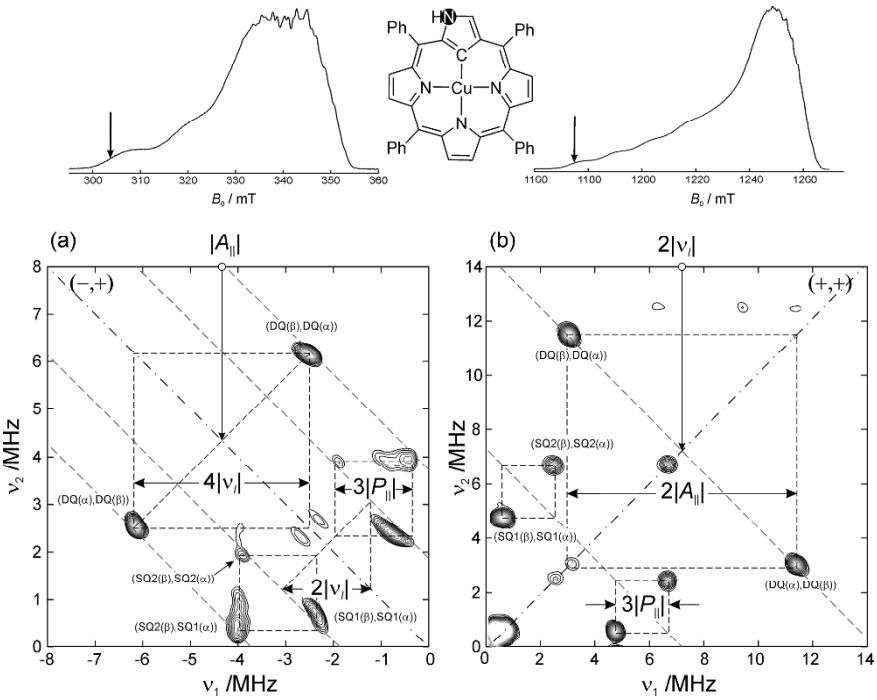

Figure 10. HYSCORE spectra of the remote ^{14}N of Cu(II)NCTPP diluted in ZnTPP powder, measured at the field positions indicated by the arrows in the field-swept spectra (upper part of figure). (a) X-band spectrum; m.w. frequency, 9.7 GHz; ν_{14N} = 0.9 MHz; τ = 100 ns. (b) Q-band spectrum; m.w. frequency, 35.6 GHz; ν_{14N} = 3.6 MHz; τ = 100 ns. All interactions are given in MHz. Modified with permission from [42]. Copyright © 2005, Wiley-VCH.

Figure 10 shows ^{14}N HYSCORE spectra from the Cu(II) N-confused tetraphenylporphyrin (NCTPP) complex measured at X- and Q-band frequencies [42]. The correlation peaks observed in the single-crystal like spectra, measured at $g_\parallel$, are assigned to the remote ^{14}N nucleus of the inverted pyrrole. In the Q-band spectrum (Fig. 10b, weak-coupling case) the stronger peaks appear in the first quadrant.

The cross-peaks representing double-quantum transitions lie on the antidiagonal at $2|\nu_I| = 7.2$ MHz and are separated by $2|A_s| \approx 8.5$ MHz, from which a hyperfine coupling of $|A_s| \approx 4.3$ MHz is estimated. The other four cross-peaks are assigned to single-quantum transitions; they exhibit a hyperfine splitting $|A_s| \approx 4.3$ MHz along the direction of the antidiagonal, and a quadrupole splitting $3|P| \approx 1.8$ MHz along the direction of the diagonal (P is the quadrupole coupling along this orientation, see [43]). Note that the estimation of the couplings is based on Eq. (8b), which is a first-order approximation, and valid only when **g**, **A**, and **P** are coaxial and $\mathbf{B}_0$ is parallel to one of the principal axes. For a more accurate estimation of parameters numerical simulations of the frequency positions are necessary.

In the X-band spectrum (Fig. 10a, strong-coupling case) the peaks appear in the second quadrant, (–,+). The double-quantum cross-peaks are separated by approximately $4|\nu_I| = 3.6$ MHz and centered around the hyperfine coupling $|A_s| \approx 4.3$ MHz. The cross-peaks close to the antidiagonal at $|A_s|/2 \approx 2.2$ MHz are assigned to single-quantum transitions. In addition, correlations between single- and double-quantum frequencies appear close to the diagonal. From the single-quantum frequencies a quadrupole splitting of $3|P| \approx 1.5$ MHz is evaluated that deviates slightly from the one estimated by the Q-band measurements. This discrepancy is related to the different orientation selection at the two m.w. frequencies. At X-band there are more orientations contributing to the experiment and the correlation ridges become broader.

The correlation patterns are more complex if the nuclear quadrupole, the hyperfine, and the nuclear Zeeman interactions are of the same order of magnitude. This situation is often encountered in X-band HYSCORE spectra of weakly coupled nitrogen nuclei in transition metal complexes. A special case, where the spectrum is considerably simplified, is the so-called exact cancellation condition, where $|A_S| \approx 2|\omega_I|$. Under this condition, the nuclear frequencies within one of the two m_S manifolds correspond to the nuclear quadrupole resonance (NQR) frequencies $\omega_0 = 2K\eta$, $\omega_- = K(3 - \eta)$, and $\omega_+ = K(3 + \eta)$ [43], which are orientation independent. Consequently, correlation peaks involving these frequencies appear as narrow features in the nuclear frequency spectrum.

Due to its high resolution, HYSCORE spectroscopy has become a powerful method for the characterization of paramagnetic metalloproteins [3–5]. Dikanov and coworkers [44] used orientation-selective ^{15}N-HYSCORE experiments to study the coordination environment of the Archaeal Rieske [2Fe–2S] center. From the HYSCORE spectra the authors were able to distinguish weak hyperfine couplings from both histidyl and peptide backbone nitrogens. Prisner and coworkers [45] used HYSCORE to investigate the environment of the 2Fe–2S (N1) cluster of complex I from *Yarrowia lipolytica*. This study revealed two sets of proton hyperfine couplings corresponding to two sets of β-protons of the cysteine ligands, and one weakly coupled nitrogen. Since the ^{14}N hyperfine and nuclear quadrupole coupling parameters were found to be very similar to those of ferredoxin-type FeS clusters, the authors assigned the ^{14}N coupling to a backbone nitrogen nucleus.

Lubitz and coworkers [46] employed HYSCORE to study the spin density distribution in the active site of [NiFe]-hydrogenase from *Desulfovibrio vulgaris* Miyazaki F in the reduced Ni–C state. Upon $H_2O \rightarrow D_2O$ exchange of the solvent, the HYSCORE spectrum contained ^2H peaks that were assigned to an exchangeable proton residing in a bridging position between nickel and iron. An exchangeable bridging proton was also found earlier in a regulatory hydrogenase [47]. The similarity of the [NiFe] centers found in catalytically active and regulatory hydrogenase suggests that their functional differences originate from structural differences further away from the [NiFe] center.

HYSCORE spectroscopy has been successfully used to study heme-containing proteins like cytochromes [48] and hemoglobins [49]. Van Doorslaer and coworkers [50] demonstrated how a combined ^1H and ^{14}N HYSCORE study can reveal structural information on the heme pocket of ferric mouse neuroglobin. They showed that the imidazole planes of the proximal (F8His) and distal (E7H) histidines bounded to the iron of the heme group are nonparallel. The good agreement of this result with available X-ray diffraction data shows that pulse EPR techniques can be confidently applied to study the arrangement of ligands in these metalloproteins.

For nuclei with $I > 1$ the analysis of HYSCORE spectra can be demanding due to their high degree of complexity. Although there are theoretical studies aimed at the understanding of basic features, no analytical solutions are available [51–53]. Therefore, an accurate interpretation depends on spectrum simulation. In a pulse EPR study of the ox1 form of methyl-coenzyme M reductase, HYSCORE spectroscopy was utilized to study the hyperfine ($A(^{33}S)$ = [10, 24, 17] MHz) and nuclear quadrupole ($|e^2qQ/h|$ = 36 MHz, $\eta = 0.1$) interactions from the thiolate sulfur group of CoM ($^{-}{}^{33}SCH_2CH_2SO_3^{-}$, ^{33}S: $I = 3/2$), which was found to bind to the nickel ion of the cofactor F_{430} [54]. The ox1 complex was formally best described as an Ni(III) (d^7) thiolate in resonance with a thiyl radical/high-spin Ni(II) complex, $Ni^{III} - {}^{-}SR \leftrightarrow Ni^{II} - {}^{\bullet}SR$. The detection of an Ni–S bond in the active site of MCR provides valuable information for proposed catalytic cycles that proceed via such or related intermediates (e.g., in one proposal the Ni(I) center attacks the thioether sulfur of methyl-CoM, generating a methyl radical and the thiolate complex CoM–S–Ni(II)F_{430} as intermediates).

3.4. Remote Echo Detection

The use of a remote-echo detector allows τ values shorter than the spectrometer deadtime τ_d to be employed [55]. This is important in two-pulse ESEEM experiments where the deadtime prevents the signal for times $\tau < \tau_d$ from being recorded. Also in the deadtime-free four-pulse experiments described in §3.3, a small τ value is often needed to avoid blind spots. Blind spots are a particular concern for the measurement of proton spectra at X-band, where the signals typically extend from 5 to 25 MHz, and with a τ = 100 ns blind spots occur at $\nu = n/\tau$ = 0, 10, 20, … MHz.

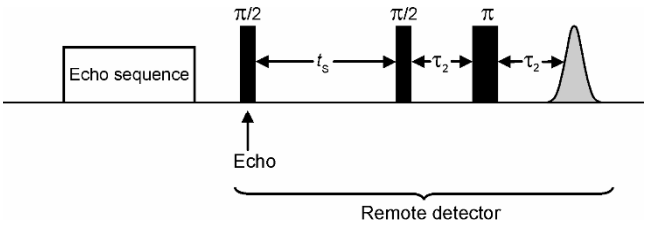

Figure 11. Pulse sequence for remote-echo detection. Modified with permission from [7]. Copyright © 2001, Oxford University Press.

The remote-echo detector is shown in Figure 11. In this method the electron spin echo at the end of the pulse sequence, which uses $\tau_1 < \tau_d$ for the nuclear coherence generator, is not recorded. Instead, at the time of echo formation an additional $\pi/2$ pulse transfers the electron coherence to longitudinal magnetization. The echo amplitude information can thus be stored for a time interval up to the order of T_1. After a fixed time delay $t_s < T_1$, the z-magnetization is read out using a two-pulse echo sequence with a fixed time interval $\tau_2 > \tau_d$. Remote echo detection can be applied to many experiments, including three-pulse ESEEM and HYSCORE, and thus can eliminate blind spots with an appropriate choice of small τ_1. Note, however, that it may suffer from reduced sensitivity due to the increased sequence time.

3.5. Matched ESEEM

An important issue in ESEEM experiments is sensitivity, which, apart from relaxation effects, is mainly determined by the modulation depth k. Equation (15) shows that for $I = ½$ nuclei the modulation depth is maximal when the hyperfine coupling is comparable to the nuclear Zeeman interaction ($|A_S| \approx |2\omega_I|$). For nuclei with very strong or very weak hyperfine interactions, and/or very small hyperfine anisotropy ($B \approx 0$), the modulation amplitude practically vanishes. An efficient sensitivity enhancement can be achieved by optimizing the strength ω_1^m and duration t_p of the m.w. pulses. These "nonideal" m.w. pulses can create nuclear coherence from electron spin polarization. The optimization of this transfer by means of the appropriate strength ω_1^m and length t_p of the nonideal m.w. pulse is called matching. Experimentally the strength ω_1 of the m.w. pulse can be satisfactorily calibrated by optimizing the primary echo intensity from a two-pulse sequence, for an $S = ½$ system $\omega_1 = g\beta_e B_1/\hbar = \pi/t_\pi$, where t_π is the length of the π pulse. For the case of very weak coupling $|A_S| << |2\omega_I|$, an optimized transfer occurs when $\omega_1^m \approx |\omega_I|$, whereas in the case of very strong coupling $|A_S| >> |2\omega_I|$, the largest enhancement is obtained with the maximum ω_1 experimentally available [56]. For instance, for weakly coupled protons at X-band, the strength of the matched m.w. pulse has to be $\omega_1^m/2\pi \approx |\omega_I|/2\pi \approx 15.6$ MHz, corresponding to a nominal $\pi/2$ pulse of 16 ns length. For strongly coupled nuclei, ω_1^m is often restricted to the maximum experimentally achievable ω_1, typically ranging between 30 and 50 MHz at X-band. The optimum length of the matched pulse is typically determined experimentally.

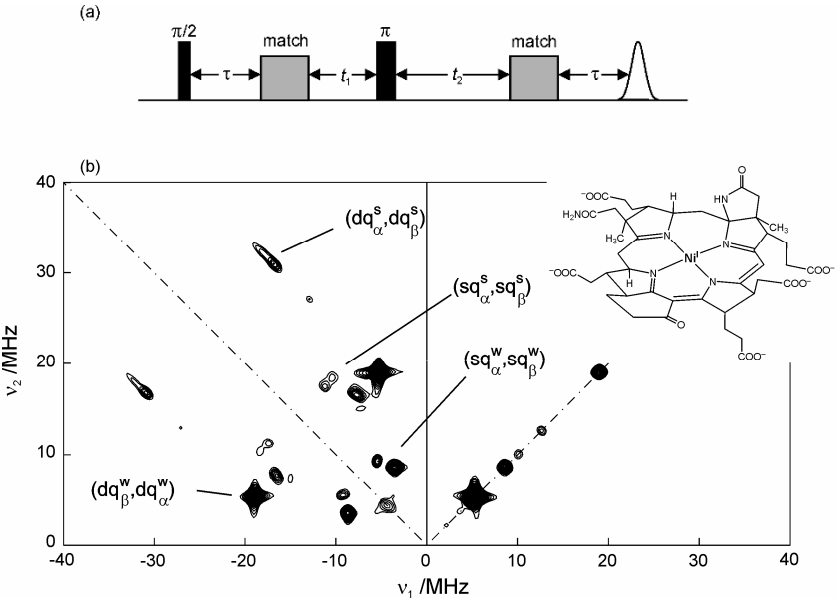

Figure 12. (a) Pulse sequence for matched HYSCORE. (b) Q-band (35.3 GHz) matched HYSCORE spectrum from the red2 species of MCR. Signals from the weakest coupled pyrrole nitrogen are labeled with superscript "w," those from the three strongest coupled pyrrole nitrogens with superscript "s." The later type of nitrogens were only observed using matched HYSCORE with m.w. pulses of strength $\omega_1/2\pi = 31.25$ MHz ($t_\pi = 16$ ns) and matched pulses of length 24 ns (nominal flip angle of $3\pi/2$). Insert: Cofactor F_{430}, in the red2 state the upper axially ligand is known from ^{33}S HYSCORE data to be the thiolate sulfur of CoM ($H^{33}SCH_2CH_2SO_3^-$). Modified with permission from [15]. Copyright © 2003, Springer.

Matched pulses can be implemented in all ESEEM experiments described here. Figure 12a shows a matched HYSCORE pulse sequence where the second and third $\pi/2$ pulses of the standard experiment have been replaced by matched pulses [57]. By using matched pulses the signal intensities can be enhanced by more than one order of magnitude as compared to standard HYSCORE.

A matched HYSCORE spectrum is shown in Figure 12b for the red2 species of methyl-coenzyme reductase (MCR), where the four pyrrole nitrogens of the porphinoid macrocycle (cofactor F_{430}) are directly coordinated to an Ni(I) ion ($S = ½$, d^9) [15]. HYSCORE measurements show that the complex has two sets of pyrrole nitrogens. One pyrrole nitrogen has hyperfine couplings of $A(^{14}N)$ = [16, 13.5, 11.8] MHz, which produces deep modulations at Q-band ($2\nu_I$ = 7.2 MHz). The other three pyrrole nitrogens, however, with hyperfine couplings in the range 20–27 MHz, give rise to a very shallow modulation depth and are thus not observable with the standard HYSCORE sequence. However, with matched pulses signals from these strongly coupled nitrogens are significantly enhanced and both double-

quantum and single-quantum transitions are observed. These data show that there is a significant electronic and/or geometric distortion of the cofactor F_{430}.

3.6. DONUT-HYSCORE

In the HYSCORE experiment only nuclear frequencies in different m_S manifolds belonging to the same paramagnetic center are correlated with each other. For multinuclear spin systems the assignment of nuclear frequencies is often not straightforward, since some of the correlation peaks may not be observed in the HYSCORE spectrum due to the small intensity of the nuclear transitions in one of the two m_S manifolds. Additional information can be gained if correlations of nuclear frequencies within the same m_S manifold can be obtained. Cross-peaks that represent such correlations can be created by replacing the nonselective transfer π pulse in the HYSCORE sequence by the double nuclear-coherence transfer (DONUT) mixer $\pi - \tau - \pi$ [58]. This DONUT-HYSCORE experiment with the pulse sequence $\pi/2 - \tau_1 - \pi/2 - t_1 - \pi - \tau_2 - \pi - t_2 - \pi/2 - \tau_1 -$ echo results in cross-peaks ($\omega_{\alpha,i}$, $\omega_{\alpha,j}$) and ($\omega_{\beta,i}$, $\omega_{\beta,j}$). The presence of these cross-peaks in the DONUT-HYSCORE spectrum is a proof that $\omega_{\alpha,i}$ and $\omega_{\alpha,j}$ belong to the same paramagnetic center, and this information can support their unambiguous assignment. An experimental example for nitrogens that are close to the exact cancellation condition has been published for the complex Co(II)TPP(py) [59], where the DONUT-HYSCORE experiment revealed one of the NQR frequencies that was missing from the HYSCORE spectrum.

3.7. Hyperfine Decoupling Techniques

The interpretation of nuclear frequency spectra can be simplified if the hyperfine interaction can be eliminated by a decoupling procedure. In principle the decoupling of the electron spin S from the nuclear spin I can be achieved using m.w. or r.f. pulses with a strength $\gamma_e B_1$ ($\gamma_n B_2$) that is larger than the hyperfine coupling. However, since the maximum technically achievable B_1 (B_2) is approximately 1 mT and the gyromagnetic ratio of the electron γ_e and nuclear γ_n spins differ by two to three orders of magnitude, it turns out that hyperfine decoupling through m.w. radiation is relatively easy, whereas decoupling through r.f. radiation is virtually impossible. For this reason hyperfine decoupling is only possible by exciting the electron spins, which are also used for detection. During hyperfine decoupling under strong resonant m.w. radiation the quantization axis of the electron spins S is rotating with the Larmor frequency in the xy-plane of the laboratory frame. The local field at nuclear spin I generated by the electron spin S thus becomes strongly time dependent and is averaged for times $t >> 2\pi/\omega_S$. In principle it is then possible to decouple the electron spin from the nuclear spin by applying a prolonged strong m.w. pulse. However, for off-resonant spin packets there will still be a nonzero component of S along $\mathbf{B}_0$, resulting in a residual hyperfine coupling. The theoreti-

cal analysis of the eigenvalues of the spin Hamiltonian under a strong m.w. pulse gives for an $S = ½$, $I = ½$ spin system [56]

$$\omega_{\alpha,\beta}^{\mathrm{dec}} = \omega_I \pm \frac{A\Omega_S}{2\omega_1} - \frac{B^2(\Omega_S{}^2 - \omega_I{}^2)}{8\omega_1{}^2\omega_I}, \tag{24a}$$

and for an $S = ½$, $I = 1$ spin system [60]

$$\begin{aligned}
\omega_{\mathrm{SQ1}(\alpha,\beta)}^{\mathrm{dec}} &= \omega_{\mathrm{SQ1}} \pm \frac{A\Omega_S}{2\omega_1} \pm \frac{A^2}{4\omega_1} + \frac{B^2}{8(\omega_I \mp \omega_1)}, \\
\omega_{\mathrm{SQ2}(\alpha,\beta)}^{\mathrm{dec}} &= \omega_{\mathrm{SQ2}} \pm \frac{A\Omega_S}{2\omega_1} \mp \frac{A^2}{4\omega_1} + \frac{B^2}{8(\omega_I \pm \omega_1)}, \\
\omega_{\mathrm{DQ}(\alpha,\beta)}^{\mathrm{dec}} &= \omega_{\mathrm{DQ}} \pm \frac{A\Omega_S}{\omega_1} + \frac{B^2\omega_I}{4(\omega_I{}^2 - \omega_1{}^2)},
\end{aligned} \tag{24b}$$

where the subscripts SQ1 and SQ2 denote the two single-quantum nuclear spin transitions (m_I, m_I+1) = (0,1) and (–1,0), and DQ the double-quantum transition, (–1,1). In Eqs. (24) the first term on the right-hand side gives the desired nuclear frequencies corresponding to complete decoupling ($A = 0$, $B = 0$), whereas the remaining terms describe the residual hyperfine splitting.

Hyperfine-decoupling methods are particularly useful when the hyperfine-decoupled spectrum is correlated to the original undecoupled spectrum in a 2D experiment [61]. The proposed hyperfine-decoupled DEFENCE [62] scheme is based on the DEFENCE sequence [24], where the third π/2 pulse is replaced by a decoupling pulse of variable length T_{dec} (Fig. 13a). This introduces a second dimension along which the hyperfine-decoupled frequencies given by Eq. (24) can be obtained. For an $S = ½$, $I = ½$ spin system this experiment correlates the two nuclear frequencies ω_α and ω_β of Eq. (12) with the corresponding decoupled frequency $\omega_{\mathrm{dec}} = \omega_{\mathrm{I}}$, so that the nuclear frequencies of different types of nuclei can be separated from each other. For the $S = ½$, $I = 1$ case, the six nuclear frequencies $\omega_{\mathrm{SQ1}(\alpha,\beta)}$, $\omega_{\mathrm{SQ2}(\alpha,\beta)}$, and $\omega_{\mathrm{DQ}(\alpha,\beta)}$ (see Fig. 2) will be correlated with the corresponding decoupled frequencies ω_{SQ1}, ω_{SQ2}, and ω_{DQ} that contain only the nuclear Zeeman and quadrupole interactions. Consequently, a direct determination of the nuclear quadrupole interaction becomes possible.

The main drawback of this pulse sequence is the residual hyperfine splitting, which causes line broadening along the decoupling dimension. For spin packets with small off-resonance frequencies ($\Omega_{\mathrm{S}} \approx 0$) narrow peaks will be obtained, but the residual hyperfine splitting arising from off-resonance spin packets scales with $\Omega_{\mathrm{S}}/\omega_1$ and thus can only be reduced by applying sufficiently strong m.w. fields. However, since a typical maximum m.w. field is around $\omega_1/2\pi = 50$ MHz, complete decoupling is not possible with currently available commercial spectrometers.

The residual hyperfine splitting can be eliminated with the pulse sequence shown in Figure 13b. In contrast to the previous pulse sequence, the nuclear coherence during the decoupling pulses evolves now in both electron spin manifolds. It

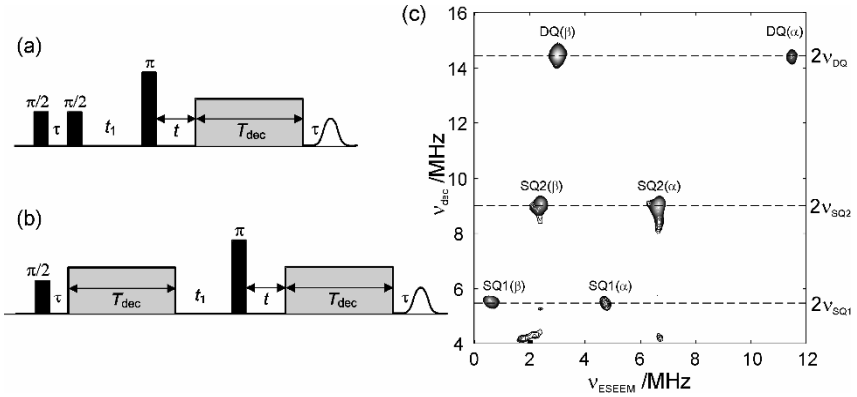

Figure 13. Pulse sequences for hyperfine-decoupled ESEEM (a,b) and 2D experimental example (c). (a) Hyperfine-decoupled DEFENCE. (b) New hyperfine-decoupled DEFENCE sequence for elimination of the residual hyperfine splitting. (c) Application of (b) on Cu(II)NCTPP diluted in Zn(TPP) powder measured at Q-band. Experimental parameters: observer position, $g_{\|}$; m.w. field strength of decoupling pulses, $\omega_1 \approx 32$ MHz; $\tau = 140$ ns; $t_1 = 170$ ns; starting value for t, $t_0 = 96$ ns incremented in steps of $\Delta t = 16$ ns; starting value for T_{dec}, $T_0 = 16$ ns incremented in steps of $\Delta T_{dec} = 8$ ns (256 × 512 datapoints).

is then expected, in analogy with the combination peak experiment [24], also that the frequencies $\omega_{\pm}^{dec} = \left|\omega_{\alpha}^{dec} \pm \omega_{\beta}^{dec}\right|$ will appear in the decoupling dimension of the spectrum. For the weak hyperfine coupling case ($2|\omega_I| > |A_S|$) with $I = ½$, for every off-resonance spin packet the decoupled frequencies are in first order symmetrically placed around ω_I, so that the sum-combination frequency, $\omega_{+}^{dec} = 2\omega_I$, is free from secular residual hyperfine contributions. Similarly, for $I = 1$, the six nuclear frequencies are correlated with the three sum-combination frequencies:

$$\begin{aligned}
\omega_{SQ1(\alpha)}^{dec} + \omega_{SQ1(\beta)}^{dec} &= 2\omega_{SQ1} - B^2\omega_I / 4\omega_I^2, \\
\omega_{SQ2(\alpha)}^{dec} + \omega_{SQ2(\beta)}^{dec} &= 2\omega_{SQ2} - B^2\omega_I / 4\omega_I^2, \\
\omega_{DQ(\alpha)}^{dec} + \omega_{DQ(\beta)}^{dec} &= 2\omega_{DQ} - B^2\omega_I / 2\omega_I^2.
\end{aligned} \tag{25}$$

For sufficiently strong m.w. fields the terms containing the nonsecular hyperfine coupling B can be neglected and the sum-combination frequencies become twice the completely decoupled frequencies.

The remarkable reduction of the residual hyperfine coupling by using this new decoupling scheme has been demonstrated by numerical simulations and experimental results [60]. Its application on Cu(II)NCTPP performed at the observer position $g_{\|}$ ($B_0 = 1174$ mT) is shown in Figure 13c. The correlation peaks observed in the 2D plot are assigned to the remote nitrogen ($\nu_N = 3.6$ MHz) of the inverted pyrrole. The nuclear frequencies in the ESEEM dimension correspond to those observed in the HYSCORE spectrum of Figure 10b. The double-quantum frequencies $\nu_{DQ(\alpha)}$ and $\nu_{DQ(\beta)}$ are correlated with $2\nu_{DQ} = 14.4$ MHz. The single-quantum fre-

quencies $\nu_{SQ1(\alpha)}$ and $\nu_{SQ1(\beta)}$ are correlated with $2\nu_{SQ1} = 5.4$ MHz, whereas the other two $\nu_{SQ2(\alpha)}$ and $\nu_{SQ2(\beta)}$ are correlated with $2\nu_{SQ2} = 9.0$ MHz. The narrow peaks along the decoupling dimension allow for an accurate estimation of the completely decoupled frequencies $\nu_{SQ1} = 2.7$ MHz, $\nu_{SQ2} = 4.5$ MHz and $\nu_{DQ} = 7.2$ MHz. With these frequencies we find $|\nu_{SQ2} - \nu_{SQ1}| \approx 3|P| = 1.8$ MHz, which is in accordance with the value estimated from the analysis of the HYSCORE peaks. Note that with this approach the quadrupole coupling parameters can be estimated with high accuracy because ν_{SQ1}, ν_{SQ2}, and ν_{DQ} are free from hyperfine coupling parameters. The latter can then also be accurately determined from the ESEEM frequencies since they now become the only unknowns. Consequently, hyperfine decoupling experiments can be very useful for the interpretation of complicated ESEEM spectra.

4. ELECTRON NUCLEAR DOUBLE RESONANCE (ENDOR)

Apart from ESEEM methods, electron nuclear double resonance (ENDOR) spectroscopy is the other well-established technique for measuring nuclear transition frequencies of paramagnetic compounds. We start with a brief discussion of the two standard pulse schemes, Davies and Mims ENDOR, before moving onto 2D sequences aimed at resolution improvement.

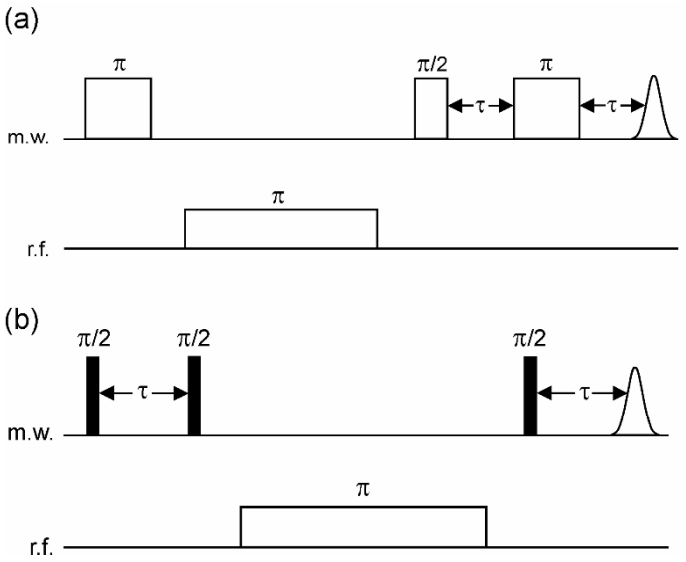

Figure 14. Pulse sequence for the Davies ENDOR (a) and Mims ENDOR (b) experiments. The inter-pulse delays are kept constant while the radio frequency is incremented over the desired frequency range. Modified with permission from [7]. Copyright © 2001, Oxford University Press.

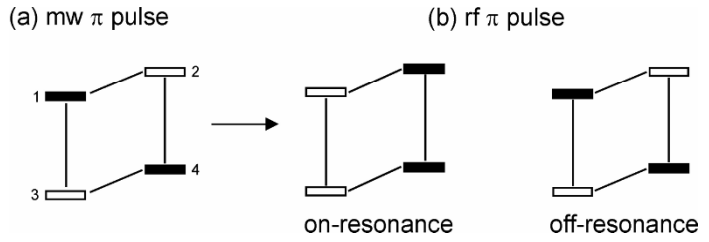

Figure 15. Populations of the energy levels of a two-spin system during the Davies ENDOR experiment: (a) selective m.w. π pulse inverts the polarization of EPR transition (1,3), (b) population after the r.f. π pulse, on-resonance with nuclear transition (1,2), or off-resonance (no effect).

4.1. Mims and Davies ENDOR

Figure 14 shows the Davies [63] and Mims [64] ENDOR pulse sequences, both of which are based on the transfer of polarization between electron and nuclear transitions.

In Davies ENDOR the first *selective* m.w. π pulse inverts the polarization of a particular EPR transition (Fig. 15a). During the mixing period a *selective* r.f. π pulse is applied. If the r.f. pulse is resonant with one of the nuclear frequencies (Fig. 15b), the polarization of this transition is inverted, which also alters the polarization of the electron spin echo observer transition (1,3) detected via a primary echo, $\pi/2 - \tau - \pi - \tau -$ echo. The ENDOR spectrum is thus recorded by monitoring the primary echo intensity as the r.f. frequency is incremented stepwise over the desired frequency range.

The first m.w. pulse in Davies ENDOR is required to be selective, for example, in Figure 15a the m.w. pulse must only invert the population of level (1,3) and not (2,4). The inversion pulse can therefore be used as a filter by varying the pulse length and thus the selectivity. This concept can be used at X-band when weakly coupled proton signals overlap with strongly coupled nitrogen signals. An example is given in Figure 16, where traces 1 and 3 were measured with a relatively selective m.w. π pulse of length 200 ns, whereas traces 2 and 4 were measured with a short, and thus less selective, m.w. pulse of length 32 ns. This has the effect of attenuating signals from the weakly coupled protons (A_S < 10 MHz), while signals from the strongly coupled nitrogen nuclei (A_S ~ 30 MHz) are enhanced relative to the protons. The absolute ENDOR intensity as a function of the selectivity parameter η_s is given by [65]

$$V(\eta_S) = V_{max} \frac{\sqrt{2}\eta_S}{\eta_S^2 + 1/2} \text{ with } \eta_S = a_{iso} t_{mw} / 2\pi , \tag{26}$$

where V_{max} is the maximum ENDOR intensity obtained with $\eta_S = \sqrt{2}/2$ and t_{mw} is the length of the first m.w. π pulse.

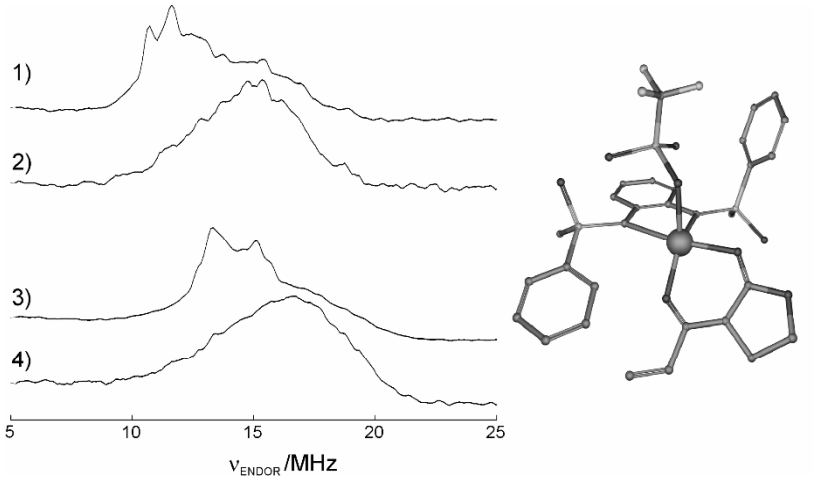

Figure 16. Hyperfine contrast selective X-band Davies ENDOR spectra of the Cu(II) bis(sulfoximine) complex (right) measured near $g_{\parallel}$ (traces 1 and 2) and $g_{\perp}$ (traces 3 and 4). Traces 1 and 3 were recorded using a π pulse of length 200 ns, traces 2 and 4 with a π pulse of length 32 ns to suppress the weakly coupled protons. The strongly coupled ^{14}N nuclei (trace 2 and 4) are centered at one-half of the hyperfine coupling, $A_S/2$, between 14.5 and 17 MHz. Modified with permission from [66]. Copyright © 2003, American Chemical Society.

Mims ENDOR is based on the stimulated echo sequence with three nonselective m.w. π/2 pulses (Fig. 14b). The preparation part, $\pi/2 - \tau - \pi/2$, creates a τ-dependent grated polarization pattern. During the mixing period, the polarization is changed by a selective r.f. pulse if it is on-resonance with a nuclear frequency. The electron polarization is then detected via a stimulated echo created at time τ after the last π/2 m.w. pulse. The ENDOR efficiency is given by [64]

$$F_{\text{ENDOR}} = \tfrac{1}{4}\left(1 - \cos(A_S\tau)\right), \tag{27}$$

and depends upon the hyperfine coupling constant A_S and the time τ. It is maximum for $\tau = (2n + 1)\pi/A_S$, and zero for $\tau = 2n\pi/A_S$, with (n = 0, 1, 2, …). Mims ENDOR thus exhibits a blind-spot behavior similar to three-pulse ESEEM, but which now depends upon A_S (in three-pulse ESEEM the blind spots depend upon ω_α and ω_β).

The τ dependence of the signal can be used to enhance signals from weakly coupled nuclei. An example is shown in Figure 17 for the case of weakly coupled ^{19}F nuclei [66]. The complete set of spectra show the expected pattern for a pure dipole interaction, with the splitting along $g_{\parallel}$ ($2T$) being approximately twice as large as the splitting along $g_{\perp}$ (T). Using the point-dipole model [Eq. (4)] with a T = 0.57 MHz allows the average electron–fluorine distance of 0.5 nm to be estimated. With this information the coordination of the triflate anion to the copper ion can be inferred, as shown on the right of Figure 17. Significantly, these data are

uniquely obtained by EPR on a sample prepared with the relevant catalytic conditions (e.g., the bis(sulfoximine) Cu(II) catalyst in solution with the solvent CH_2Cl_2). Therefore, information is obtained on the subtle influence of counterions and solvent molecules on the efficiency and steroselectivity of the catalytically induced C–C bond forming reaction.

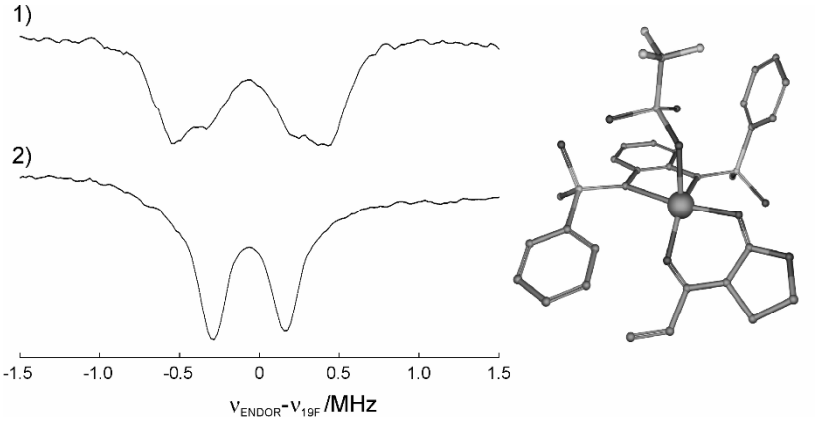

Figure 17. ^{19}F W-band Mims ENDOR spectra of the Cu(II) bis(sulfoximine) complex (right) measured at $g_{\|}$ (trace 1) and $g_{\perp}$ (trace 2). Due to the small ^{19}F hyperfine interaction and considering the phase memory time T_M, the optimum sensitivity was obtained with τ = 400 ns. The ^{19}F signals originate from the triflate anion. Modified from [66]. Copyright © 2003. American Chemical Society.

For nuclei with large hyperfine couplings and large anisotropies the τ dependence of the signal can produce unwanted blind spots in the spectrum. Note that the deadtime of the spectrometer prevents very small τ values from being used: at X-band typically τ is 100 ns or more. For τ = 100 ns blind spots occur when A_S = 0, 10, 20, … MHz. For large hyperfine couplings it is thus usually preferable to employ the Davies ENDOR sequence with a well-chosen length for the m.w π pulse [Eq. (26)]. Conversely, Mims ENDOR can be particularly sensitive for measuring small hyperfine couplings if the phase memory time T_M of the sample is sufficiently long to allow an optimal τ value to be used. The blind spot behavior in Mims ENDOR can be avoided with a remote-echo detection sequence [55] or with the refocused Mims ENDOR approach [67].

4.2. Baseline Artifacts in ENDOR

A significant technical problem in ENDOR arises from r.f. heating, resulting in small changes in the resonator tuning, and leading to the appearance of baseline artifacts in the ENDOR spectrum. This problem is most severe at low temperatures, but can be overcome by varying the r.f. frequency acquisition not linearly, but randomly [68]. Convincing examples are shown in [68].

4.3. Hyperfine-Correlated ENDOR Spectroscopy

The resolution of the basic 1D Mims and Davies ENDOR sequences can be improved by disentangling the spectrum into a second appropriately chosen dimension. One approach is to correlate the ENDOR frequencies with their corresponding hyperfine frequencies, so-called hyperfine-correlated ENDOR spectroscopy. We discuss two sequences that achieve this correlation: 2D Mims ENDOR and HYEND (hyperfine correlated ENDOR).

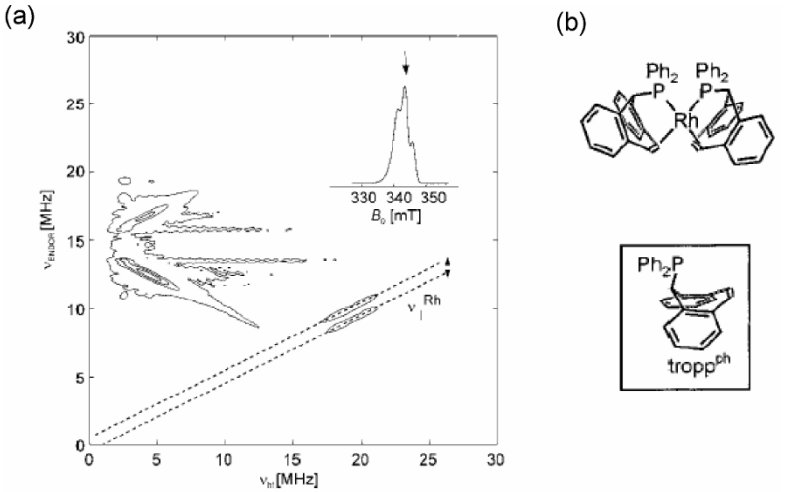

Figure 18. (a) Two-dimensional Mims ENDOR spectrum of [Rh(tropp^{ph})$_2$]. The dashed lines are separated by $2\nu_I$(Rh) and cross the ν_{hf} and ν_{ENDOR} axes at ν_I(Rh). Proton signals are centered around ν_{ENDOR} = 15 MHz and have hyperfine couplings up to ~ 10 MHz. Inset: EPR spectrum, the arrow indicates the observer position used for the ENDOR experiment. (b) Structure of [Rh(tropp^{ph})$_2$] and the tropp^{ph} ligand. Modified with permission from [69]. Copyright © 2002, Editions Scientifiques Elsevier.

The 1D Mims ENDOR sequence can readily be extended to include a hyperfine dimension by incrementing, in addition to the r.f. frequency, the τ value. Equation (27) shows that the ENDOR efficiency oscillates with $\cos(A_S\tau)$, and thus performing a FT of the time-domain traces recorded as a function of τ results in a hyperfine-correlated ENDOR spectrum. An example is shown in Figure 18 for the complex [Rh(tropp^{ph})$_2$], which has rhodium (I = ½) hyperfine couplings in the range 16–21 MHz [69].

2D Mims ENDOR is restricted to hyperfine couplings smaller than the frequency range covered by the m.w. pulses, typically <50 MHz, and can suffer from poor resolution along the hyperfine axis as the signal decays with the phase memory time T_M (which is often of the order of only a few microseconds in transition metal complexes).

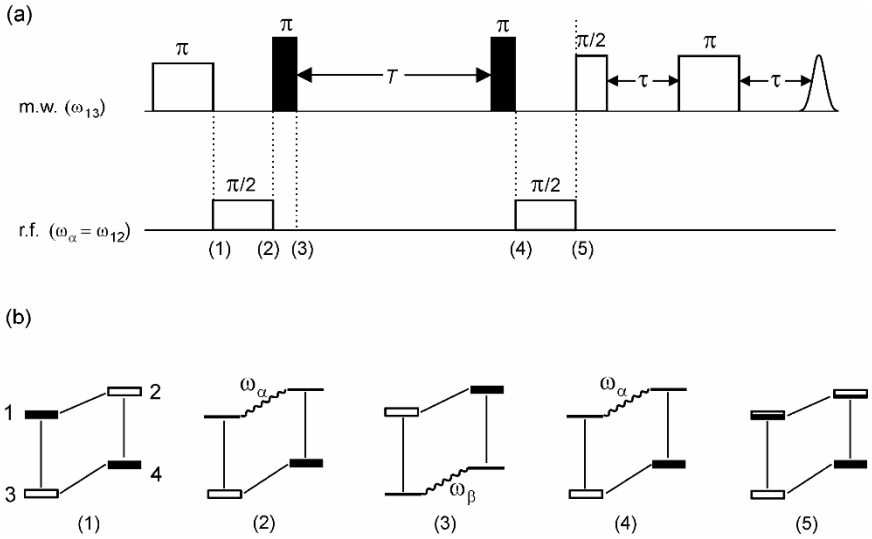

Figure 19. HYEND experiment. (a) Pulse sequence. (b) Four-level energy diagrams for an $S = ½$, $I = ½$ spin system illustrating the different states obtained during the experiment. Modified with permission from [7]. Copyright © 2001, Oxford University Press.

The HYEND experiment [70] also correlates ENDOR frequencies with their corresponding hyperfine couplings. The pulse sequence is show in Figure 19a. The nuclear frequency dimension is obtained by varying the frequency of the two selective π/2 r.f. pulses, and the hyperfine dimension by the FT of the echo modulations recorded as a function of the time T. The states attained during the experiment for an $S = ½$, $I = ½$ spin system are shown in Figure 19b. The experiment is easily understood qualitatively. We assume that the first m.w. pulse is on resonance with the allowed EPR transition (1,3) and the r.f. pulse has the frequency ω_α and is thus resonant with the nuclear transition (1,2). The first m.w. pulse inverts the polarization of transition (1,3), and the selective r.f. pulse transfers the polarization of transition (1,2) to nuclear coherence (wavy line). This coherence is immediately transferred by a nonselective m.w. π pulse to the β electron spin manifold, where it evolves with the nuclear frequency ω_β for a time T. The second nonselective m.w. π pulse transfers the nuclear coherence back to the α manifold, where the second r.f. pulse transfers the nuclear coherence back to electron polarization, which is detected with the m.w. primary echo sequence. The two r.f. pulses must remain coherent during the sequence, and then the polarization created by the second r.f. pulse is dependent upon the phase accumulated by the nuclear coherence during the time T in the β manifold with respect to the phase of the r.f field. This phase is given by $(\omega_\alpha + \omega_\beta)T$ (weak coupling) or $(\omega_\alpha - \omega_\beta)T$ (strong coupling). The HYEND signal as a function of T, for an isotropic hyperfine interaction with the r.f. pulses resonant with a nuclear transition, is given by

$$V_{\alpha/\beta}(T) = \pm \operatorname{sign}(2\omega_I + a_{iso})\cos(\omega_- T) \text{ with } \omega_- = \omega_\alpha - \omega_\beta = a_{\text{iso}}. \quad (28)$$

Figure 20 illustrates a HYEND spectrum from a [Rh(trop$_2$NCH$_2$)(PPh$_3$)] complex [71], which demonstrates the resolution of ^{13}C and ^{103}Rh signals that are otherwise difficult to assign in an X-band Davies ENDOR experiment.

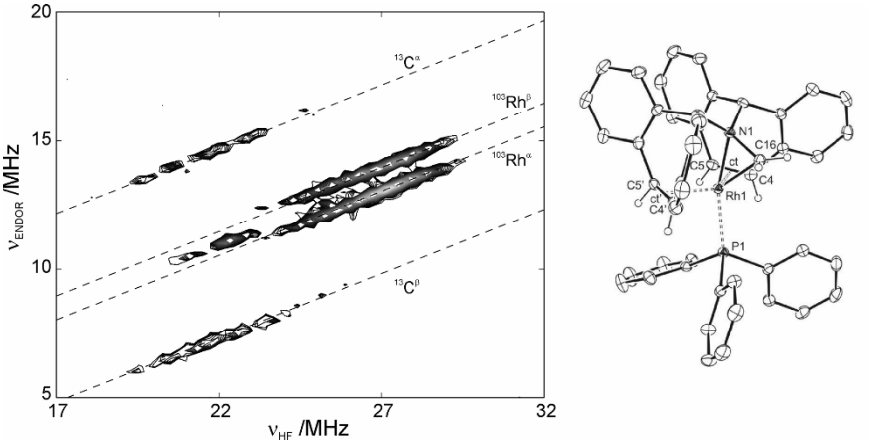

Figure 20. X-band HYEND spectrum of [Rh(trop$_2$NCH$_2$)(PPh$_3$)] in THF measured at 15 K. The dashed lines are separated by twice the nuclear Zeeman interaction ($2\nu_I$) of ^{103}Rh and ^{13}C, and cross the ν_{ENDOR} and ν_{hf} axes at $\nu_I(^{103}\text{Rh})$ and $\nu_I(^{13}\text{C})$, respectively. Modified with permission from [71]. Copyright © 2006, Wiley-VCH.

4.4. Triple Resonance

This experiment is usually employed to determine the relative sign of two hyperfine couplings [72], or in the 2D version additionally the relative orientation between two hyperfine tensors [73,74]. In a triple resonance (or double ENDOR) experiment, the nuclear transitions are excited with two r.f. fields. Figure 21a shows the pulse sequence based on the Davies ENDOR approach. The mixing time now consists of two r.f. π pulses separated by a time ΔT. The first r.f. pulse (pump pulse) with frequency ω_{rf1} must be resonant with a particular nuclear transition, while the frequency ω_{rf2} of the second r.f. pulse (scan pulse) is swept through the ENDOR spectrum. Figure 21b shows the expected spectra for an $S = ½$, $I_1 = ½$, $I_2 = ½$ spin system in the weak coupling case ($A_{1S} > A_{2S} > 0$, $\omega_{I1} = \omega_{I2}$): the ENDOR spectrum (top), the triple spectrum (middle) when the pump pulse is resonant with peak 1, and the difference triple spectrum (bottom) obtained by subtraction. Since peak 2 occurs on the same side of ω_I as the pump pulse on peak 1, the two hyperfine couplings have the same sign. The difference spectrum contains only transitions that belong to the same electron spin manifold of the same paramagnetic center.

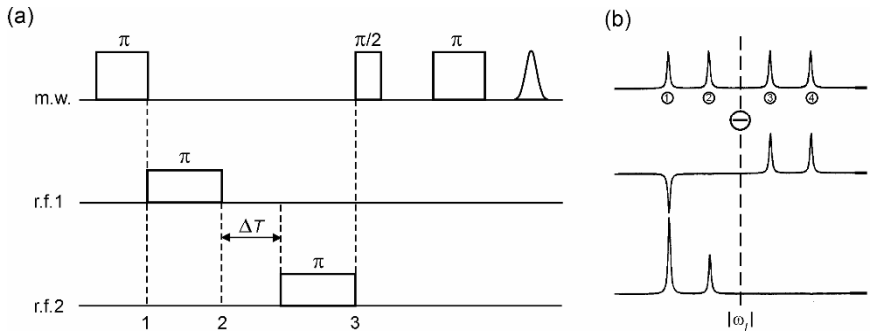

Figure 21. (a) Pulse sequence for the triple resonance experiment. (b) ENDOR spectrum (top), triple spectrum (middle), and difference triple spectrum (bottom). Modified with permission from [7]. Copyright © 2001, Oxford University Press.

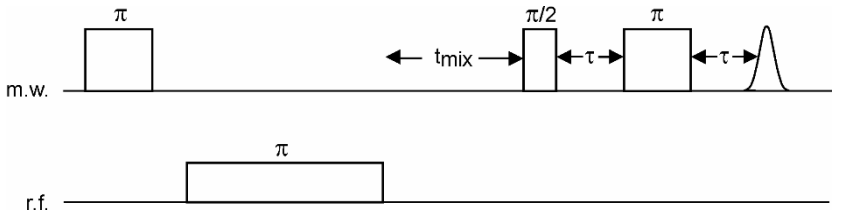

Figure 22. Pulse sequence for the variable mixing-time ENDOR experiments based on the Davies ENDOR sequence. Under suitable conditions the asymmetry of the ENDOR spectrum depends upon the variable mixing time t_{mix}, and the sign of the hyperfine coupling.

4.5. Variable Mixing Time ENDOR

Variable mixing time ENDOR experiments can be used to determine the absolute sign of a hyperfine coupling [75]. One such sequence based on Davies ENDOR is shown in Figure 22 [76], and includes an additional variable mixing time (VMT), t_{mix}. Under suitable conditions the ENDOR signals from the two electron spin manifolds become distorted (asymmetric), with the asymmetry depending upon the electron and nuclear spin-lattice relaxation and cross-relaxation times, T_{1e}, T_{1n}, and T_{1x}, respectively, the thermal polarization, and the sign of the hyperfine coupling. Under suitable experimental conditions, usually low temperature and high field, the sign of the hyperfine coupling can be determined from the relative intensity of the ENDOR signals from the two m_S manifolds. Epel and colleagues [77] provice an example of this approach using ^{1}H W-band ENDOR on frozen solutions of nitrous oxide reductase (N_2OR).

4.6. High-Field ENDOR

The advantages of measuring ENDOR spectra at high field are (1) separation of signals of nuclei with different γ_n, (2) increased orientation selectivity, (3) increased sensitivity for samples when only a small amount of material is available or where it is only possible to grow small single crystals, (4) improved resolution of paramagnetic centers with different g-values, and hence their ENDOR spectra, (5) spectra with low γ_n can be measured, such as ^{2}H nuclei, (6) simplification of spectra from high-spin systems where the electron Zeeman interaction is dominant, and (7) it is often possible to determine the absolute sign of the hyperfine interaction.

Points 1 and 2 can be easily appreciated by inspection of the spin Hamiltonian given in Eq. (1); the electron and nuclear Zeeman interactions are field dependent. For this reason overlapping spectra of different types of nuclei can be separated at higher B_0 fields. For instance, at X-band frequencies (e.g., B_0 = 330 mT), the ENDOR spectra of weakly coupled ^{1}H and ^{19}F nuclei overlap since they are approximately centered at ν_H = 14 MHz and ν_F = 13.2 MHz, respectively. By measuring at W-band frequencies (e.g., B_0 = 3300 mT) the difference between ν_H = 140 MHz and ν_F = 132 MHz might be sufficient to separate the two signals. Another example, often encountered in X-band ENDOR spectra of transition metal complexes, is the overlap of strongly coupled ^{14}N signals centered at $A_S/2 \approx$ 15 MHz and weakly coupled ^{1}H signals centered at $\nu_H \approx$ 14 MHz (see Fig. 16). At higher m.w. frequencies (e.g., Q-band, $\nu_H \approx$ 50 MHz) the two signals can be fully separated.

In the case of strongly coupled nuclei with $I > ½$, the measurement at higher B_0 fields can improve resolution because of the increased nuclear Zeeman splitting. An example is shown in Figure 23 for the Cu(II) complex of N-confused tetraphenylporphyrin. The Davies ENDOR spectra measured close to $g_{\|}$ (Fig. 23a) consist of doublets split by $2\nu_{14N}$ and centered at ν_{ENDOR} = 30 MHz. Consequently, these peaks are assigned to strongly coupled nitrogens of the porphyrin core. Due to the unresolved nuclear quadrupole interaction along this orientation, the resolution enhancement gained by going from X- to Q-band frequencies does not provide any further information. The situation is different for the observer position at $g_{\perp}$. The X-band Davies ENDOR spectrum (Fig. 23b, left) consists of five peaks corresponding to the turning points of the orientation dependent single-quantum nuclear frequencies (Fig. 23c, left). These four frequencies strongly overlap because the nuclear Zeeman and quadrupole splittings are comparable ($2\nu_{14N}$ = 2.1 MHz, $3P \approx$ 2.8 MHz). In going to Q-band frequency (Fig. 23b, right) the nuclear Zeeman splitting increases to $2\nu_{14N}$ = 7.6 MHz, and this results in an almost complete separation of the nitrogen signals from the two electron spin manifolds (Fig. 23c, right). This resolution enhancement allows for a more straightforward spectrum simulation [42].

In going to higher B_0 fields, the resolution of ENDOR signals belonging to the same type of nucleus of the same paramagnetic species only improves as a result of the increased orientation selection (less contributing orientations equates to sharper

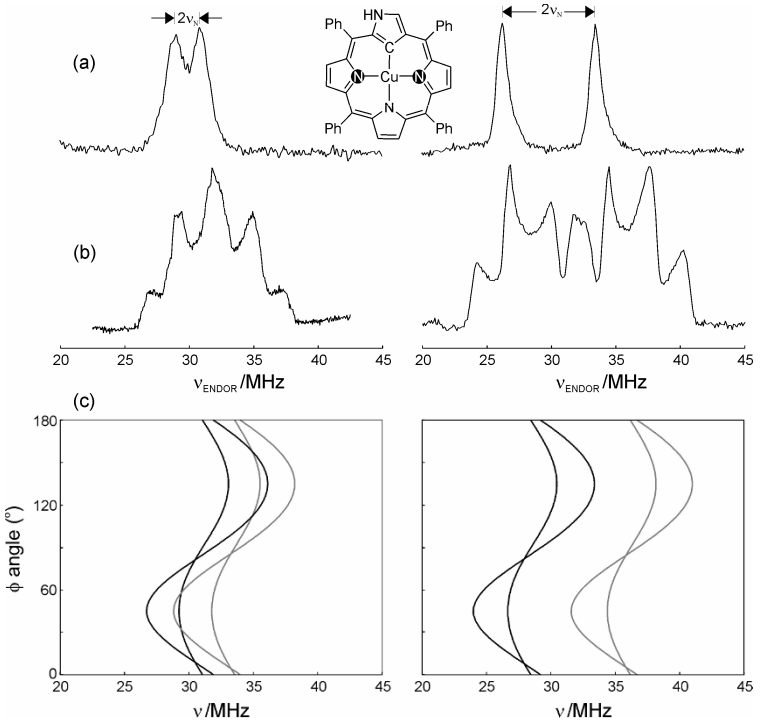

Figure 23. Comparison between X-band (left) and Q-band (right) Davies ENDOR spectra of Cu(II)NCTPP diluted in ZnTPP powder. (a) Single-crystal like spectra measured at $g_{\|}$ ($\mathbf{B}_0$ perpendicular to the porphyrin plane). The peaks are centered at 30 MHz and split by $2\nu_N$; therefore, they are assigned to the two magnetically equivalent strongly coupled core nitrogens with a hyperfine coupling of 60 MHz and an unresolved nuclear quadrupole interaction along this orientation. (b) Spectra measured at observer positions corresponding to $g_{\perp}$ ($\mathbf{B}_0$ in the porphyrin plane). (c) Theoretical in-plane ($\theta = \pi/2$) orientation dependence of the single-quantum nuclear frequencies upon the polar angle ϕ. Black curves: α electron spin manifold; gray curves: β electron spin manifold. Simulation parameters: (A_1, A_2, A_3) = (71.5, 58.3, 59.5) MHz and (P_1, P_2, P_3) = (-0.87, 1.00, -0.13) MHz, ν_N = 1.05 MHz for X-band (left) and ν_N = 3.80 MHz for Q-band (right). Modified with permission from [42]. Copyright © 2005, Wiley-VCH.

lines). However, this resolution improvement is often very modest, particularly for transition metal complexes where the *g* anisotropy is already resolved at X- or Q-band. A 2D experiment can help in these cases, and the best resolution may be achieved at lower m.w. frequencies. This is especially true for overlapping proton signals where HYSCORE [59], or the ENDOR equivalent HYSCORE-ENDOR, is ideal for separating overlapping proton signals which originate from hyperfine interactions with different anisotropies. This is because the signal shifts from the antidiagonal line are proportional to the hyperfine anisotropy and inversely proportional to the proton Larmor frequency [Eq. (23)]. A lower B_0 field also offers an

additional advantage for strongly coupled, low γ_n nuclei, since a very short r.f. π pulse can be realized as a result of the hyperfine enhancement effect (see §4.7).

4.7. Hyperfine Enhancement of r.f. Pulses

A significant technical challenge in ENDOR is to produce a strong r.f. B_2 field at the location of the sample. The effective r.f. field $B_{rf}^{eff}(t)$ that induces transitions at the nucleus is enhanced by the hyperfine interaction between the electron and the nuclear spin, an effect called hyperfine enhancement. For an isotropic hyperfine interaction and with $B_2 << B_0$, the component of $\mathbf{B}_{hf}$ perpendicular to $\mathbf{B}_0$ can be written as $B_{hf}^{\perp} = a_{iso}/(\omega_I B_2)$, and the total oscillating field amplitude B_2^{eff} with the enhancement factor E as [78]

$$B_2^{eff} = EB_2 \quad \text{with} \quad E = \left| 1 + \frac{m_s a_{iso}}{\omega_I} \right| . \tag{29}$$

More general formulae for first-order line intensities, which include hyperfine enhancement, are given in [78–81]. Pronounced hyperfine enhancements (or de-enhancements) are often found in transition metal complexes with ligand nuclei having large hyperfine couplings in comparison to their gyromagnetic ratios. This is often the case at X-band for strongly coupled nitrogens. For example, a nitrogen with a hyperfine coupling of $A_S/2\pi = 40$ MHz, $m_s = \pm½$, and $\nu_I = 1$ MHz, has a hyperfine enhancement factor of $E_\pm = 21, 19$. Practically, this means that a π r.f. pulse can be achieved in a time much shorter than would otherwise be the case, an advantage. Note that this effect will decrease at higher B_0 fields; at W-band $\nu_I = 10$ MHz and the hyperfine enhancement factor is $E_\pm = 1, 3$ for $A_S/2\pi = 40$ MHz. This effect shows that ENDOR performed at low B_0 fields is sometimes advantageous because of the higher sensitivity afforded by a larger effective B_2.

Equation (29) shows that for low-frequency transitions, where $A_s \approx 2|\omega_I|$, one of the E values is close to zero so that it becomes exceedingly difficult to excite these nuclear transitions. In this case ESEEM methods are required.

4.8. Time-Domain ENDOR

In this section we describe selected time-domain ENDOR experiments where the free evolution of nuclear coherence is recorded. These experiments consist of at least three building blocks: a nuclear coherence generator, a free evolution period for the nuclear coherence, and a nuclear coherence detector.

Time-Domain ENDOR methods often employ a chirp r.f pulse; a pulse with a linearly swept frequency. This approach enables broadband excitation of the nuclear transitions that covers the entire frequency range of the ENDOR spectrum, often of the order of 30 MHz. Note that with the available r.f. power this broad excitation range is not possible without the r.f. frequency sweep (i.e., a π r.f pulse of around 10 ns would be required, whereas a length of around 10 μs is typically needed for protons).

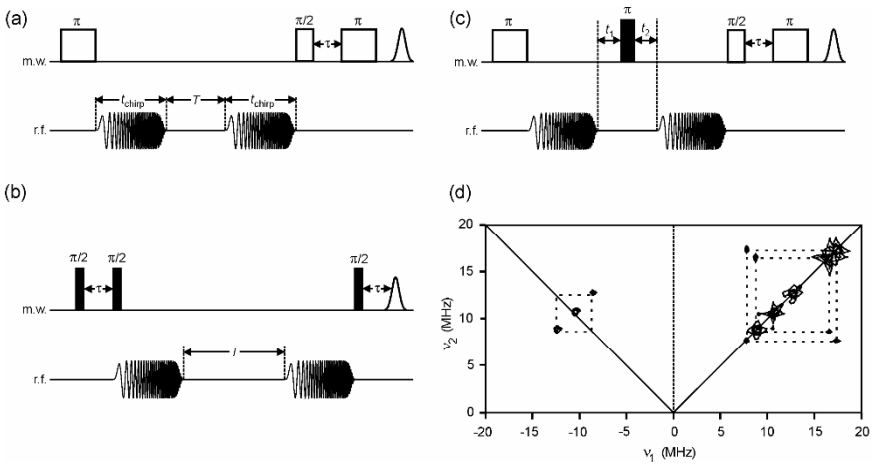

Figure 24. Sequences for chirp ENDOR experiments: (a) Davies-type chirp ENDOR; (b) Mims-type chirp ENDOR; (c) Chirp-ENDOR-HYSCORE sequence; and (d) Two-dimensional chirp ENDOR-HYSCORE spectrum of a Cu(II)-doped glycine single-crystal. Cross-peaks in the first quadrant correspond to proton ENDOR lines, cross-peaks in the second quadrant to nitrogen ENDOR lines. Modified with permission from [7]. Copyright © 2001, Oxford University Press.

The pulse sequences for a Davies-type, a Mims-type, and a Chirp-ENDOR-HYSCORE are shown in Figure 24 [82]. In the Davies-type sequence (a), the nuclear coherence generator consists of the first m.w. and r.f. chirp pulse, followed by a variable free evolution time *T*, and the nuclear coherence detector consisting of the second r.f. chirp pulse and the m.w. primary echo sequence. The time-domain trace is thus measured by incrementing *T* and recording the echo intensity. FT gives the ENDOR spectrum. The Mims-type sequence, shown in Figure 24b, functions in a similar way.

Figure 24c shows an ENDOR "equivalent" to HYSCORE, the Chirp-ENDOR-HYSCORE sequence. This sequence is based on the Davies-type chirp sequence, but with the addition of the m.w. π pulse during the free evolution time of the nuclear coherence. As with HYSCORE, the π pulse transfers nuclear coherences between the electron spin manifolds, and FT of the echo intensity as a function of the two evolution times t_1 and t_2, gives a 2D spectrum correlating the nuclear frequencies of the different electron spin manifolds, exactly as in a HYSCORE experiment. A 2D chirp-ENDOR-HYSCORE spectrum of a copper complex is shown in Figure 24d, and shows peaks from strongly coupled nitrogens in the second quadrant and from weakly coupled protons in the first quadrant. This method thus enables a clear separation of the nitrogen and proton signals, in contrast to a conventional 1D Davies ENDOR spectrum, where they overlap. ENDOR-HYSCORE is complementary to conventional HYSCORE, since ENDOR is ideal for measuring large hyperfine couplings and isotropic hyperfine couplings, and

can measure signals when $\mathbf{B}_0$ is along a principal axis direction. Conversely, in ESEEM the modulation depth vanishes for isotropic hyperfine couplings (strictly true for $I = ½$) and when $\mathbf{B}_0$ is along a principal value, and the m.w. pulses must have a sufficient bandwidth to excite both allowed and forbidden transitions of the same spin packet. The excitation bandwidth usually restricts ESEEM techniques to hyperfine interactions <50 MHz.

5. FIELD-SWEPT EPR EXPERIMENTS

This class of experiments involves measuring a field-swept EPR spectrum, either with CW excitation or using m.w. pulses. A variety of 2D pulse field-swept EPR experiments exist that aim to increase the resolution by the addition of a second dimension to the B_0 sweep; T_1 and T_2 filtered EPR [83], forbidden-transition-labeled EPR (FORTE) [84], anisotropy-resolved EPR [85], and magic-angle spinning EPR [86]. Here only two types of experiments are discussed: nutation and electron Zeeman-resolved EPR.

5.1. Nutation Experiments

It is not always possible to evaluate the electron spin quantum number S of a paramagnetic species from the field-swept EPR spectrum. Often only the ($|-½\rangle$, $|+½\rangle$) EPR transitions can be observed, or several species with different S values contribute to the spectrum. Under suitable conditions S can be determined from the nutation frequency ω_{nut}. If the m.w. radiation excites only a single transition then

$$\omega_{nut}(m_s, m_s + 1) = \frac{g_1 \beta_e B_1}{\hbar}\left[S(S+1) - m_s(m_s+1)\right]^{1/2}. \tag{30}$$

B_1 can be determined separately in a calibration experiment with a standard sample such as DPPH ($S = ½$, $g = g_1 = 2.0036$), and g_1 is related to the laboratory frame x-axis [7].

Nutation experiments allow for the measurement of very low g-values, for example, in a Ti^{3+}-doped sapphire sample $g_\perp = 0.04$ was measured by nutation spectroscopy [87]. Separation of the allowed and forbidden EPR transitions can be achieved in a 2D nutation experiment (one axis has the B_0 field sweep and the other the nutation frequencies), since allowed transitions have a significantly lower nutation frequency than the forbidden transitions [88]. A 2D nutation experiment also allows spectra from different sites in a single crystal to be separated, as for example in single crystals of N,N′-ethylenebis-(acetylacetonatiminato)Cu(II) [89]. There are several pulse sequences available to measure nutation frequencies (see, e.g., [90,91]). We explain briefly the PEANUT sequence given in Figure 25a [88]. The sequence begins with a $\pi/2$ pulse whose length determines the frequency range of the spins involved in the experiment. The transverse magnetization excited by this

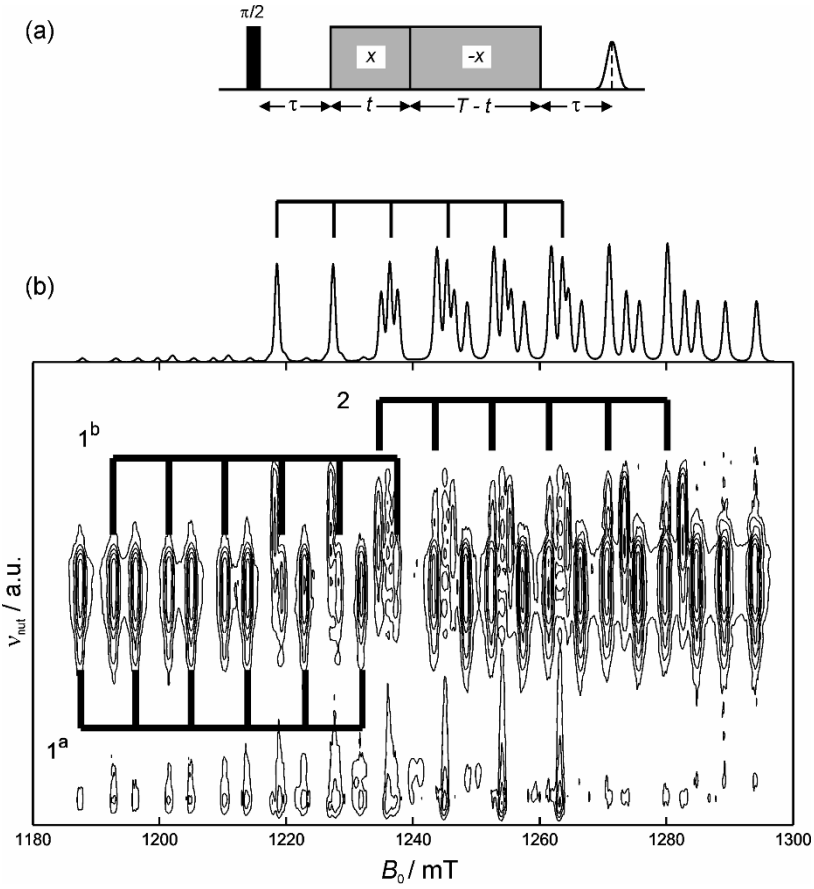

Figure 25. (a) PEANUT sequence for the measurement of nutation frequencies. (b) Peanut experiment at Q-band (35.3 GHz) on a single crystal of $Zn(Im)_6$ doped with 0.4% Mn(II) (S = 5/2, I = 5/2). Labels 1^a,1^b show the ($|-5/2,m_I\rangle$, $|-3/2,m_I\rangle$) transitions for the two sites in the single crystal. Label 2 shows the ($|+3/2,m_I\rangle$, $|+1/2,m_I\rangle$) transitions for site **a** in the single crystal, the six lines from site **b** are approximately 2 mT to the right of this pattern. Inset: FID-detected EPR spectrum with the ($|-1/2,m_I\rangle$, $|+1/2,m_I\rangle$) transitions marked. From data provided by Dr. Inés García Rubio.

pulse evolves and defocuses during the evolution period τ. Next, a pulse of constant length T, which is subdivided into two parts of variable length t and $T - t$ with opposite m.w. phases applied. During time t the B_1 m.w. field is orientated along the x-axis and the magnetization nutates with frequency ω_{eff} around an effective field B_{eff}, while during time $T - t$ the B_1 m.w. field is orientated along the minus x-axis and the magnetization nutates with the same frequency ω_{eff} but around an effective field B'_{eff}. The phase shift at time t causes a partial refocusing to a rotary echo, which is detected via a spin-locked echo formed at time τ after the nutation

pulse. A single time-domain trace is thus obtained by measuring at a fixed field position and varying the time t during the nutation pulse of constant length T. A 2D spectrum is obtained by sweeping B_0.

Figure 25b shows a PEANUT spectrum measured at Q-band (35.3 GHz) on a single crystal of $Zn(Im)_6$ doped with 0.4% Mn(II) ($S = 5/2$, $I = 5/2$ spin system). The sample contains molecules in two slightly different orientations due to the twinning of the crystal. The magnetic field sweep is along the x-axis, and the y-axis plots the nutation frequencies. The transition moment between the various m_S-manifolds depends on m_S, which results in slightly different turning angles for the ($|\pm5/2,m_I\rangle$, $|\pm3/2,m_I\rangle$), ($|\pm3/2,m_I\rangle$, $|\pm1/2,m_I\rangle$), and ($|-1/2,m_I\rangle$, $|+1/2,m_I\rangle$) transitions. In this way the different transitions can be identified in the PEANUT experiment by their position on the nutation axis. The most intense lines in the spectrum correspond to the transitions ($|\pm5/2,m_I\rangle$, $|\pm3/2,m_I\rangle$). At a higher nutation frequency the transitions ($|\pm3/2,m_I\rangle$, $|\pm1/2,m_I\rangle$) can be observed, and also, very weakly, the transitions ($|-1/2,m_I\rangle$, $|+1/2,m_I\rangle$). The upper spectrum corresponds to the FID-detected spectrum of the single crystal sample for the same crystal orientation.

5.2. Electron Zeeman-Resolved EPR

This 2D EPR experiment makes use of the fact that the electron Zeeman interaction is the only relevant field-dependent term in the spin Hamiltonian. The pulse sequence is shown in Figure 26a, and consists of a primary echo sequence together with a sinusoidal varying magnetic field, $\Delta B_0(t)$, directed along the B_0 axis. The additional magnetic field causes an accumulation of the phase of electron coherence, so that transitions with different g-values will be separated from one another. An example of this approach to disentangle a spectrum from a powder sample with an axial g-matrix and hyperfine interaction from an $I = 3/2$ nucleus is given in Figure 26b [92].

6. STRATEGIES AND OUTLOOK

In this review we have concentrated on explaining the basic mechanisms behind ENDOR and ESEEM spectroscopy. These two methods, along with field-swept EPR experiments, provide a means to obtain a detailed description of the EPR parameters of paramagnetic centers in single crystals, powders, and frozen solutions. To obtain the most accurate EPR parameters requires not one technique, but a combination, and preferably applied at several m.w. frequencies. Measurements at multi-frequencies allow possible ambiguities that arise from data measured at only one m.w. frequency to be resolved.

For ESEEM experiments in particular, the B_0 field strength needs to be matched to the hyperfine interaction of interest; the largest echo envelope modulation occurs when the nuclear Zeeman and hyperfine interaction are equal in magnitude (strictly true only for $I = ½$ nuclei). For a nucleus with a particular hyperfine interaction, the modulation depth may be too weak to observe at X-band,

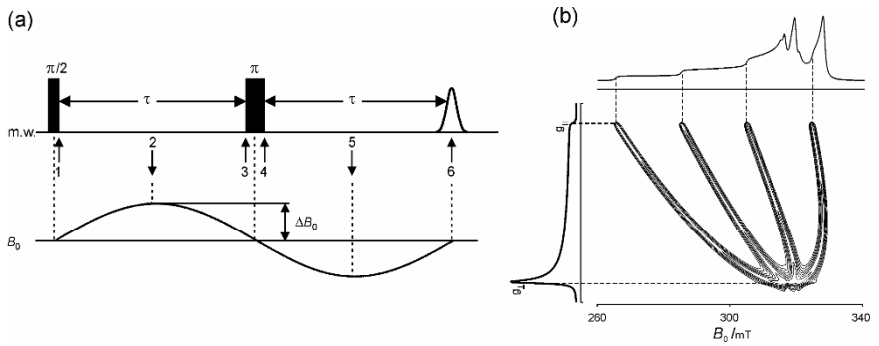

Figure 26. (a) EZ-EPR experiment consisting of a primary echo sequence and a sinusoidal $\mathbf{B}_0$ variation; (b) model calculation for an $S = ½$, $I = 3/2$ spin system. Modified with permission from [7]. Copyright © 2001, Oxford University Press.

whereas at Q-band the sensitivity can be maximum. Even when the modulation depth is predicted to be low for a particular nucleus, sensitivity improvements can conveniently be achieved by using matched pulses with an optimal m.w. field strength and length.

Generally, ENDOR resolution is superior at higher B_0 fields. However, for nuclei with low γ_n values and large hyperfine couplings, the sensitivity may be better at lower fields (X-band) because the ENDOR enhancement effect allows very short π r.f. pulses to be used. Additionally, the EPR spectrum is less spread out and thus more orientations contribute to the measurement. At lower B_0 fields, overlapping signals from different nuclei can be disentangled by 2D ENDOR experiments. Several possibilities have been described here.

Spectrum simulation is an integral part of EPR spectroscopy of disordered systems. To obtain the most accurate EPR parameters, it is usually necessary to measure (ENDOR or ESEEM) spectra at a number of observer positions across the EPR spectrum. Ideally, spectra at enough field positions should be recorded so that the set contains signals from all orientations of the paramagnetic center with respect to B_0. The number required depends on the width of the EPR spectrum. In disordered systems spectra taken away from the "single-crystal" positions consist of ridges whose width reflects the anisotropy of the spin Hamiltonian parameters, and the orientation selection. Sharp peaks are usually observed at "single-crystal" positions, which generally makes their interpretation straightforward. Once the data have been collected, each field position needs to be correctly interpreted and the signals simulated. For time-domain experiments, usually a computer programme based on the density matrix formalism [93] is implemented. Examples include EasySpin [94,95] and XSophe [96,97], and programmes by Madi et al. [31] and Shane et al. [98]. 1D time-domain experiments, such as two- or three-pulse ESEEM, can be simulated quickly with this approach. This allows in some situations a fitting algorithm to be implemented. However, simulation of 2D experiments such as HYSCORE are very time consuming, particularly if $S > ½$, if more than one nu-

clear spin needs to be considered, and for nuclei with $I > ½$. In these cases, we suggest that a scan of possible solutions first be undertaken by computing just the frequency positions of the cross-peaks by exact diagonalization of the spin Hamiltonian. This calculation is very rapid, and the correct orientation selection can be included. Once possible solutions are found, they should be checked with a simulation that includes both position and intensity information. For ENDOR, very often simulation programs calculate the nuclear frequencies and transitions by diagonalization of the spin Hamiltonian, an approach appropriate for resonant irradiation. In this case appropriate care should be taken when comparing this simulation to pulse ENDOR spectra (e.g., blind spots, hyperfine enhancement, pulse selectivity).

ACKNOWLEDGMENTS

This work was supported by the Swiss *National Science Foundation*. We acknowledge our collaborators: Prof. Hansjörg Grützmacher, Laboratory of Inorganic Chemistry, Department of Chemistry and Applied Biosciences, ETH-Zürich, 8093 Zürich, Switzerland (*Rh chemistry*); Prof. Dr. R. K. Thauer, Max Planck Institute for Terrestrial Microbiology, Department of Biochemistry, Karl-von-Frisch-Straße, 35043 Marburg, Germany, and Prof. Dr. B. Jaun, Laboratory of Organic Chemistry, Department of Chemistry and Applied Biosciences, ETH Zürich, 8093 Zürich, Switzerland (*MCR*). We thank all members of the EPR group at ETH for their support.

REFERENCES

1. Hoffman BM. 2003. ENDOR of metalloenzymes. *Acc Chem Res* **36**:522–529.
2. Hoffman BM. 2003. Electron-nuclear double resonance spectroscopy (and electron spin-echo envelope modulation spectroscopy) in bioinorganic chemistry. *Proc Natl Acad Sci USA* **100**:3575–3578.
3. Deligiannakis Y, Louloudi M, Hadjiliadis N. 2000. Electron spin echo envelope modulation (ESEEM) spectroscopy as a tool to investigate the coordination environment of metal centers. *Coord Chem Rev* **204**:1–112.
4. Lakshmi KV, Brudvig GW. 2001. Pulsed electron paramagnetic resonance methods for macromolecular structure determination. *Curr Opin Struc Biol* **11**:523–531.
5. Prisner T, Rohrer M, MacMillan F. 2001. Pulsed EPR spectroscopy: biological applications. *Annu Rev Phys Chem* **52**:279–313.
6. Goldfarb D, Arieli D. 2004. Spin distribution and the location of protons in paramagnetic proteins. *Annu Rev Biophys Biomol Struct* **33**:441–468.
7. Schweiger A, Jeschke G. 2001. *Principles of pulse electron paramagnetic resonance*. Oxford: Oxford UP.
8. *Spin density* $\rho(x,y,z)$ denotes the difference in the number of electrons per unit volume having spin up and down: $\rho(x,y,z) = \rho^{\alpha}(x,y,z) - \rho^{\beta}(x,y,z)$. *Spin population* $\rho^{\psi}{}_{X}$ is interpretable as the integrated spin density $\rho(x,y,z)$ in the orbital ψ centered on nucleus x and is the difference in the populations of unpaired electrons with spin up and spin down,

$\rho^{\psi}{}_{x} = \rho^{\psi}{}_{x}{}^{\alpha} - \rho^{\psi}{}_{x}{}^{\beta}$. See Gerson F, Huber W. 2003. *Electron spin resonance spectroscopy of organic radicals*. Weinheim: Wiley-VCH Verlag.
9. McGarvey BR. 1967. The isotropic hyperfine interaction. *J Phys Chem* **71**:51–67.
10. Morton JR, Preston KF. 1978. Atomic parameters for paramagnetic-resonance data. *J Magn Reson* **30**:577–582.
11. Golding RM, Stubbs LC. 1978. Higher-order hyperfine terms in spin. *Proc Roy Soc London* **A362**:525–536.
12. McGarvey BR. 1987. In *Electronic magnetic resonance of the solid state*, p. 83. Ed JA Weil. Ottawa: Canadian Society of Chemistry.
13. Neese F, Solomon EI. 2002. Interpretation and calculation of Spin Hamiltonian parameters in transition metal complexes. In *Magnetism: molecules to materials*, IV. Ed JS Miller, M Drillon. Weinheim: Wiley-VCH Verlag.
14. Harmer J, Van Doorslaer S, Gromov I, Schweiger A. 2002. Corrin nitrogens and remote dimethylbenzimidazole nitrogen interactions in Cob(II)alamin studied with HYSCORE at X- and Q-band. *Chem Phys Lett* **358**:8–16.
15. Finazzo C, Harmer J, Jaun B, Duin EC, Mahlert F, Thauer RK, Van Doorslaer S, Schweiger A. 2003. Characterization of the MCRred2 form of methyl-coenzyme M reductase: a pulse EPR and ENDOR study. *J Biol Inorg Chem* **8**:586–593.
16. Rowan LG, Hahn EL, Mims WB. 1965. Electron-spin-echo envelope modulation. *Phys Rev* **A137**:61–71.
17. Mims WB. 1972. Envelope modulation in spin-echo experiments. *Phys Rev* **B5**:2409–2419.
18. Zweier J, Aisen P, Peisach J, Mims WB. 1979. Pulsed electron paramagnetic resonance studies of the copper complexes of transferrin. *J Biol Chem* **254**:3512–3515.
19. Lu J, Bender CJ, McCracken J, Peisach J, Severns JC, McMillin DR. 1992. Pulsed EPR studies of the type 2 copper binding site in the mercury derivative of laccase. *Biochemistry* **31**:6265–6272.
20. Dikanov SA, Shubin AA, Parmon VN. 1981. Modulation effects in the electron spin echo resulting from hyperfine interaction with a nucleus of an arbitrary spin. *J Magn Reson* **42**:474–487.
21. Stoll S, Calle C, Mitrikas G, Schweiger A. 2005. Peak suppression in ESEEM spectra of multinuclear spin systems. *J Magn Reson* **177**:93–101.
22. Dikanov SA, Samoilova RI, Kolling DR, Holland JT, Crofts AR. 2004. Hydrogen bonds involved in binding the Q_i-site semiquinone in the bc_1 complex, identified through deuterium exchange using pulsed EPR. *J Biol Chem* **279**:15814–15823.
23. Ponti A, Schweiger A. 1994. Echo phenomena in electron paramagnetic resonance spectroscopy. *Appl Magn Reson* **7**:363–403.
24. Ponti A, Schweiger A. 1995. Nuclear coherence-transfer echoes in pulsed EPR. *J Chem Phys* **102**:5207–5219.
25. Hubrich M, Jeschke G, Schweiger A. 1995. The generalized hyperfine sublevel coherence transfer experiment in one and two dimensions. *J Chem Phys* **104**:2172–2184.
26. Schossler PM. 1998. Electron paramagnetic resonance study of the copper (II) complexation with carbonate ligands in aqueous solution and at calcium carbonate surfaces. PhD thesis, No. 12669, ETH Zürich.
27. Vinck E, Van Doorslaer S. 2004. Analysing low-spin ferric complexes using pulse EPR techniques: a structure determination of bis (4-methylimidazole) (tetraphenylporphyrinato) iron (III). *Phys Chem Chem Phys* **6**:5324–5330.

28. Höfer P, Grupp A, Nebenführ G, Mehring M. 1986. Hyperfine sublevel correlation (HYSCORE) spectroscopy: a 2D ESR investigation of the squaric acid radical. *Chem Phys Lett* **132**:279–282.
29. Tyryshkin AM, Dikanov SA, Goldfarb D. 1993. Sum combination harmonics in four-pulse ESEEM spectra: study of the ligand geometry in aqua–vanadyl complexes in polycrystalline and glass matrices. *J Magn Reson* **A105**:271–283.
30. Dikanov SA, Tyryshkin AM, Bowman MK. 2000. Intensity of cross-peaks in Hyscore spectra of $S = ½$, $I = ½$ spin systems. *J Magn Reson* **144**:228–242.
31. Mádi Z, Van Doorslaer S, Schweiger A. 2002. Efficient simulation of ESEEM spectra. *J Magn Reson* **154**:181–191.
32. Stoll S. 2003. Spectral simulations in solid-state EPR. PhD thesis, No. 15059, ETH Zürich.
33. Pöppl A, Kevan L. 1996. A practical strategy for determination of proton hyperfine interaction parameters in paramagnetic transition metal ion complexes by two-dimensional HYSCORE electron spin resonance spectroscopy in disordered systems. *J Phys Chem* **100**:3387–3394.
34. Reijerse E, Dikanov SA. 1991. Electron spin echo envelope modulation spectroscopy on orientationally disordered systems: line shape singularities in $S = ½$, $I = ½$ spin systems. *J Chem Phys* **95**:836–845.
35. Dikanov SA, Bowman MK. 1995. Cross-peak lineshape of two-dimensional ESEEM spectra in disordered $S = ½$, $I = ½$ spin systems. *J Magn Reson* **A116**:125–128.
36. Thauer RK. 1998. Biochemistry of methanogenesis: a tribute to Marjory Stephenson. *Microbiology* **144**:2377–2406.
37. Goenrich M, Mahlert F, Duin EC, Bauer C, Jaun B, Thauer RK. 2004. Probing the reactivity of Ni in the active site of methyl–coenzyme M reductase with substrate analogues. *J Biol Inorg Chem* **9**:691–705.
38. Hinderberger, D, Piskorski RP, Goenrich G, Thauer RK, Schweiger A, Harmer J, Jaun B. 2006. A nickel–alkyl bond in an inactivated state of the enzyme catalyzing methane formation. *Angew Chem, Int Ed* **45**:3602–3607.
39. Pöppl A, Böttcher R. 1997. Cross peak intensities in two-dimensional four-pulse electron spin echo modulation spectra of deuterium in single crystals. *Chem Phys* **221**:53–66.
40. Dikanov SA, Xun L, Karpiel AB, Tyryshkin AM, Bowman MK. 1996. Orientationally-selected two-dimensional ESEEM spectroscopy of the Rieske-type iron–sulfur cluster in 2,4,5-trichlorophenoxyacetate monooxygenase from *Burkholderia cepacia* AC1100. *J Am Chem Soc* **118**:8408–8416.
41. Maryasov AG, Bowman MK. 2004. Hyperfine sublevel correlation (HYSCORE) spectra for paramagnetic centers with nuclear spin $I = 1$ having isotropic hyperfine interactions. *J Phys Chem* **B108**:9412–9420.
42. Mitrikas G, Calle C, Schweiger A. 2005. Asymmetric spin density distribution in the copper (II) complex of N-confused tetraphenylporphyrin: a multifrequency continuous-wave and pulse EPR study. *Angew Chem Int Ed* **44**:3301–3303.
43. The nuclear quadrupole coupling constant $K = e^2qQ/[4I(2I - 1)\hbar]$ and the asymmetry parameter $\eta = (P_x - P_y)/P_z$ are usually given in the definition of the nuclear quadrupole tensor in its principal axes system: $\mathbf{P}^d = [P_x, P_y, P_z] = [-K(1-\eta),-K(1 + \eta),2K]$, where Q is the nuclear electrical quadrupole moment and eq is the electric field gradient.
44. Iwasaki T, Kounosu A, Uzawa T, Samoilova RI, Dikanov SA. 2004. Orientation-selected ^{15}N-HYSCORE detection of weakly coupled nitrogens around the archaeal Rieske [2Fe–2S] center. *J Am Chem Soc* **126**:13902–13903.

45. Maly T, Grgic L, Zwicker K, Zickermann V, Brandt U, Prisner T. 2006. Cluster N1 of complex I from *Yarrowia lipolytica* studied by pulsed EPR spectroscopy. *J Biol Inorg Chem* **11**:343–350.
46. Foerster S, van Gastel M, Brecht M, Lubitz W. 2005. An orientation-selected ENDOR and HYSCORE study of the Ni–C active state of *Desulfovibrio vulgaris* Miyazaki F hydrogenase. *J Biol Inorg Chem* **10**:51–62.
47. Brecht M, van Gastel M, Buhrke T, Friedrich B, Lubitz W. 2003. Direct detection of a hydrogen ligand in the [NiFe] center of the regulatory H_2-sensing hydrogenase from *Ralstonia eutropha* in its reduced state by HYSCORE and ENDOR spectroscopy. *J Am Chem Soc* **125**:13075–13083.
48. García-Rubio I, Martínez JI, Picorel R, Yruela I, Alonso PJ. 2003. HYSCORE Spectroscopy in the cytochrome b_{559} of the photosystem II reaction center. *J Am Chem Soc* **125**:15846–15854.
49. Ioanitescu AI, Dewide S, Kiger L, Marden MC, Moens L, Van Doorslaer S. 2005. Characterization of nonsymbiotic tomato hemoglobin. *Biophys J* **89**:2628–2639.
50. Vinck E, Van Doorslaer S, Dewilde S, Mitrikas G, Schweiger A, Moens L. 2006. Analyzing heme proteins using EPR techniques: the heme-pocket structure of ferric mouse neuroglobin. *J Biol Inorg Chem* **11**:467–475.
51. Gutjahr, M, Böttcher, R, Pöppl A. 2002. Analysis of correlation patterns in hyperfine sublevel correlation spectroscopy of $S = 1/2$, $I = 3/2$ systems. *Appl Magn Reson* **22**:401–414.
52. Matar K, Goldfarb D. 1992. Fourier transform electron spin echo envelope modulation of a $S = 1/2$, $I = 5/2$ spin system: an exact analysis and a second order perturbation approach. *J Chem Phys* **96**:6464–6476.
53. Ponti A. 1997. Electron-spin-echo envelope modulation arising from hyperfine coupling to a nucleus of arbitrary spin. *J Magn Reson* **127**:87–104.
54. Harmer J, Finazzo C, Piskorski R, Bauer C, Jaun B, Duin EC, Goenrich M, Thauer RK, Van Doorslaer S, Schweiger A. 2005. Spin density and coenzyme M coordination geometry of the ox1 form of methyl-coenzyme M reductase: a pulse EPR study. *J Am Chem Soc* **127**:17744–17755.
55. Cho H, Pfenninger S, Gemperle C, Schweiger A, Ernst RR. 1989. Zero deadtime pulsed ESR by remote echo detection. *Chem Phys Lett* **160**:391–395.
56. Jeschke G, Schweiger A. 1996. Generation and transfer of coherence in electron-nuclear spin systems by non-ideal microwave pulses. *Mol Phys* **88**:355–383.
57. Jeschke G, Rakhmatullin R, Schweiger A. 1998. sensitivity enhancement by matched microwave pulses in one- and two-dimensional electron spin echo envelope modulation spectroscopy. *J Magn Reson* **131**:261–271.
58. Goldfarb D, Kofman V, Libman J, Shanzer A, Rahmatouline R, Van Doorslaer S, Schweiger A. 1998. Double nuclear coherence transfer (DONUT)-HYSCORE: a new tool for the assignment of nuclear frequencies in pulsed EPR experiments. *J Am Chem Soc* **120**:7020–7029.
59. Van Doorslaer, S, Bachmann, R, Schweiger, A. 1999. A pulse EPR and ENDOR investigation of the electronic and geometric structure of cobaltous tetraphenylporphyrin (pyridine). *J Phys Chem* **A103**:5446–5455.
60. Mitrikas G, Schweiger A. 2004. Hyperfine decoupling in electron paramagnetic resonance as a powerful tool for unraveling complicated ESEEM spectra of $S = ½$, $I \geq ½$ systems. *J Magn Reson* **168**:88–96.

61. Jeschke, G, Schweiger A. 1997. Hyperfine decoupling in electron spin resonance. *J Chem Phys* **106**:9979–9991.
62. Van Doorslaer S, Schweiger A. 1999. New hyperfine-decoupling schemes in electron paramagnetic resonance spectroscopy. *Chem Phys Lett* **308**:187–194.
63. Davies ER. 1974. New pulse ENDOR technique. *Phys Lett* **A47**:1–2.
64. Mims WB. 1965. Pulsed ENDOR experiments. *Proc Roy Soc London* **283**:452.
65. Fan C, Doan PE, Davoust CE, Hoffman B. 1992. Quantitative studies of Davies pulsed ENDOR. *J Magn Reson* **98**:62–72.
66. Bolm C, Martin M, Gescheidt G, Palivan C, Neshchadin D, Bertagnolli H, Feth M, Schweiger A, Mitrikas G, Harmer J. 2003. Spectroscopic investigations of bis(sulfoximine) copper(II) complexes and their relevance in asymmetric catalysis. *J Am Chem Soc*:**125**, 6226–6227.
67. Doan PE, Hoffman B. 1997. Making hyperfine selection in Mims ENDOR independent of deadtime. *Chem Phys Lett* **269**:208–214.
68. Epel B, Arieli D, Baute D, Goldfarb D. 2003. Improving W-band pulsed ENDOR sensitivity-random acquisition and pulsed special TRIPLE. *J Magn Reson* **164**:78–83.
69. Deblon S, Liesum L, Harmer J, Schönberg H, Schweiger A, Grützmacher H. 2002. High-resolution EPR spectroscopic investigations of a homologous set of d^9-cobalt(0), d^9-rhodium(0), and d^9-iridium(0) complexes. *Chem Eur J* **8**:601–611.
70. Jeschke G, Schweiger A. 1995. Hyperfine-correlated electron-nuclear double-resonance spectroscopy. *Chem Phy Lett* **246**:431–438.
71. Maire P, Sreekanth A, Büttner T, Harmer J, Gromov I, Rüegger H, Breher F, Schweiger A, Grützmacher H. 2006. Synthesis of a rhoda-aza-cyclopropane and characterization of its radical cation by EPR. *Angew Chem, Int Ed* **45**:3265–3269.
72. Mehring M, Höfer P, Grupp A. 1987. Pulsed electron nuclear double and triple resonance schemes. *Ber Bunsenges Phys Chem* **91**:1132–1137,.
73. Epel B, Goldfarb D. 2000. Two-dimensional pulsed TRIPLE at 95 GHz. *J Magn Reson* **146**:196–203.
74. Sammet A, Hubrich M, Spiess HW. 1995. Nature and dynamics of radicals in polyaramide as studied by pulsed electron nuclear double resonance. *Adv Mater* **7**:747–750.
75. Bennebroek MT, Schmidt J. 1997. Pulsed ENDOR spectroscopy at large thermal spin populations and the absolute sign of the hyperfine interaction. *J Magn Reson* **128**:199–206.
76. Epel B, Pöppl A, Manikandan P, Vega S, Goldfarb D. 2001. The effects of spin relaxation on the ENDOR spectra recorded at high magnetic fields and low temperatures. *J Magn Reson* **148**:388–397.
77. Epel B, Manikandan P, Kroneck PMH, Goldfarb D. 2001. High-field ENDOR and the sign of hyperfine coupling. *Appl Magn Reson* **21**:287–297.
78 Abragam A, Bleaney B. 1970. *Electron paramagnetic resonance of transition ions*, §4.3, Oxford: Oxford UP.
79. Schweiger A. Günthard HsH. 1982. Transition-probabilities in electron nuclear double-resonance and multiple-resonance spectroscopy with noncoherent and coherent radio-frequency fields. *Chem Phys* **70**:1–22.
80. Schweiger A, Günthard HsH. 1981. Electron nuclear double-resonance with circularly polarized radio-frequency fields (CP-ENDOR): theory and applications. *Mol Phys* **42**:283–295.
81. Schweiger A. 1982. Electron nuclear double-resonance of transition metal complexes with organic ligands. *Struct Bonding* **51**:1–119.

82. Jeschke G, Schweiger A. 1995. Time-domain chirp electron nuclear double-resonance spectroscopy in one and 2 dimensions, *J Chem Phys* **103**:8329–8337.
83. Maly T, MacMillan F, Zwicker K, Kashani-Poor N, Brandt U, Prisner TF. 2004. Relaxation filtered hyperfine (REFINE) spectroscopy: a novel tool for studying overlapping biological electron paramagnetic resonance signals applied to mitochondrial complex I. *Biochemistry* **43**:3969–3978.
84. Willer M, Schweiger A. 1994. Forbidden-transition-labeled EPR (FORTE): an approach for the sensitive measurement of forbidden EPR transitions. *Chem Phys Lett* **230**:67–74.
85. Sierra G, Schweiger A. 1998. Anisotropy-resolved electron paramagnetic resonance spectroscopy. *Mol Phys* **95**:973–987.
86. Hessinger D, Bauer C, Hubrich M, Jeschke G, Spiess HW. 2000. Magic-angle sample spinning electron paramagnetic resonance: instrumentation, performance, and limitations. *J Magn Reson* **147**:217–255.
87. Willer M, Schweiger A. 1997. Determination of *g* values by a new electron spin transient nutation experiment: the $g_{\perp}$ value of titanium-doped sapphire. *Chem Phys Lett* **264**:1–8.
88. Stoll S, Jeschke G, Willer M, Schweiger A. 1998. Nutation-frequency correlated EPR spectroscopy: the PEANUT experiment. *J Magn Reson* **130**:86–96.
89. Astashkin AV, Schweiger A. 1990. Electron-spin transient nutation: a new approach to simplify the interpretation of ESR spectra. *Chem Phys Lett* **174**:595–602.
90. Mizuochi N, Ohba Y, Yamauchi S. 1997. A two-dimensional EPR nutation study on excited multiplet states of fullerene linked to a nitroxide radical. *J Phys Chem* **A101**:5966–5968.
91. Kouskov V, Sloop DJ, Liu SB, Lin TS. 1995. Pulsed transient nutation experiments on the photoexcited triplet-state. *J Magn Reson Series* **A117**:9–15.
92. Sierra GA. 1997. Two-dimensional pulse electron spin resonance methods for spectral resolution enhancement in solids. PhD thesis, No. 12241, ETH Zürich.
93. Blum K. 1981. Density matrix theory and applications. New York: Plenum.
94. See http://www.esr.ethz.ch
95. Stoll S, Schweiger A. 2006. EasySpin, a comprehensive software package for spectral simulation and analysis in EPR. *J Magn Reson* **178**:42–55.
96. Wang D, Hanson GR. 1996. New methodologies for computer simulation of paramagnetic resonance spectra. *Appl Magn Res* **11**:401–415.
97. Noble CJ, Benson, S, Hanson GR. 2007. Molecular Sophe: an integrated approach to the structural characterization of paramagnetic molecules. *Biol Magn Reson* **28**. In press.
98. Shane JJ., Liesum LP, Schweiger A. 1998. Efficient simulation of ESEEM spectra using gamma. *J Magn Reson* **134**:72–75.